Characterization and Simulation of a CdTe detector for use in PET

Master Thesis

Universitat Autònoma de Barcelona (UAB)

Institut de Física d'Altes Energies (IFAE)

Author:
Gerard Ariño Estrada

Director:
Prof. Mokhtar Chmeissani

Supervisor:
Dr. Gianluca de Lorenzo

September 13, 2012

This work has been supported by FP7-ERC-Advanced Grant #250207

Abstract

The Voxel Imaging PET (VIP) Pathfinder project got the 4 year European Research Council FP7 grant in 2010 to prove the feasibility of using CdTe detectors in a novel conceptual design of PET scanner. The work presented in this thesis is a part of the VIP project and consists of, on the one hand, the characterization of a CdTe detector in terms of energy resolution and coincidence time resolution and, on the other hand, the simulation of the setup with the single detector in order to extend the results to the full PET scanner.

An energy resolution of 0.98% at 511 keV with a bias voltage of 1000 V/mm has been measured at low temperature T=-8$°C$. The coincidence time distribution of two twin detectors has been found to be as low as 6 ns FWHM for events with energies above 500 keV under the same temperature and bias conditions. The measured energy and time resolution values are compatible with similar findings available in the literature and prove the excellent potential of CdTe for PET applications.

This results have been presented in form of a poster contribution at the IEEE NSS/MIC & RTSD 2011 conference in October 2011 in Valencia and at the iWoRID 2012 conference in July 2012 in Coimbra, Portugal. They have been also submitted for publication to “Journal of Instrumentation (JINST)” in September 2012.

Acknowledgments

This thesis would never have been written, at least not by me, if I weren't a member of the VIP team and I owe this to Mokhtar Chmeissani: thank you the confidence you are putting on me from the first day of the project, when I didn't know even what a LEMO cable is.

This thesis is just a part of the work the whole VIP team has done in the last two years and so I have to thank the help of all its components. Thank you very much for all this silent help. I want to thank in particular: Machiel, thank you for being always ready to help me, even knowing that at the end I'll tell you it's your fault! Jose, gracias por todo el tiempo que dedicas en mi, por todas las explicaciones sin las que no hubiera podido sacar adelante esta tesis y por ser, no sólo en el trabajo, otro hermano mayor and Gianluca, grazie mille per la pazienza nella supervisione e per l'enorme e indispensabile aiuto che mi hai dato in tutto questo tempo per me sei come il quarto fratello maggiore. Spero ricompensarti insegnandoti qualche colpo di squash!

Aprofito l'ocasió per agrair també, més enllà de l'àmbit professional, a tots els que fan que la meva vida a Barcelona sigui alguna cosa més que només agradable (perdoneu que no us citi però no voldria deixar-me a ningú). Agraeixo especialment als qui han de sentir a parlar d'aquest projecte (segurament) més del que els tocaria, pel fet de viure amb mi: Dany, July i Tony. Gràcies també als que des de l'Ebre intenten no perdre'm de vista. Menció a part mereixen ma mare i mun germà Jordi, un suport com lo vostre fa molt més fàcil enfrontar qualsevol situació en la vida, no m'imagino com faria este camí sense vatros.

Per acavar, gràcies a la Bona Sort, per guiar-me en cada petit trèbol que fa crèixer al meu voltant.

Contents

Introduction

The analysis described in this thesis has been carried on within the Voxel Image PET (VIP) Pathfinder, an ambitious project with the aim of proving the feasibility of constructing a Positron Emission Tomography (PET) scanner from pixelated CdTe detectors. The characterization of a single CdTe detector, fundamental unit of the full system, is of crucial importance to correctly define the specifics of the future device and to drive the development of the different components and sub-systems. In particular, the values of the energy and time resolution, and, more in detail, a correct model of the charge collection and the signal formation process, are needed for a fine tuning of the full system simulation from which the expected performance of the novel design is assessed. A dual effort involving laboratory measurements and the development and tuning of simulation codes are therefore necessary and are the object of this work.

After defining the laboratory working conditions to be as close as possible to the expected working conditions of the final device, three main experiments have been conducted: the measurement of the electron and hole mobilities, the measurement of the energy resolutions at 122 keV and 511 keV, and the measurement of the coincidence time resolution of two twin CdTe detectors operating in coincidence. The measured values of 0.98% full width at half maximum (FWHM) for the energy resolution at 511 keV and of 6 ns FWHM for the time resolution are in perfect agreement with similar results documented in literature and proves that CdTe detectors are indeed excellent candidates to be the preferred detection medium of the next generation PETs.

In parallel, the full setup has been simulated and results from Monte Carlo experiments have been compared to the real data in order to tune the model parameters. The non negligible discrepancies resulting from the comparison between the real data and the preliminary results from simulation have been analyzed and possible explanations are now driving the on going effort to further improve the underlying models.

The thesis is made of three main chapters. The first one is an introduction to the physics principle behind the semiconductor diode detectors. The second chapter is dedicated to the description of the experimental setup and the different measurements. Chapter 3 gives an overview of the simulation technique and a preliminary comparison between simulation and real data. Finally the last chapter of the thesis presents some conclusions and a brief discussion of the future developments.

Chapter 1

Theoretical Overview

1.1 Semiconductor Diode Detectors

Devices employing semiconductors as the basic detection medium became practically available in the early 1960s. Early versions were called crystal counters, but modern detectors are referred to as semiconductor diode detectors or simply solid-state detectors. Although the latter term is somewhat ambiguous in the sense that technically scintillation counters can also be thought of as solid-state detectors, it has come into widespread use to characterize only those devices that are based on electron-hole pair collection from semiconductor media.

Semiconductor detectors offer many desirable features such as high energy resolution, compact size, relatively fast timing characteristics and an effective thickness that can be varied to match the requirements of the preferred application.

1.1.1 Band Structure in Solids

The periodic lattice of crystalline materials establishes allowed energy bands for electrons that exist within that solid. The energy of any electron within the pure material must be confined to one of these energy bands, which may be separated by gaps or ranges of forbidden energies. A simplified representation of the bands of interest in insulators or semiconductors is shown in Fig. 1.1. The lower band, called the valence band, corresponds to those outer-shell electrons that are bound to specific lattice sites within the crystal. The next higher-lying band is called the conduction band and represents electrons that are free to migrate through the crystal, electrons in this band contribute to the electrical conductivity of the material. The two bands are separated by the bandgap, the size of which determines whether the material is classified as a semiconductor or an insulator. The number of electrons within the crystal is just adequate to fill completely all available sites within the valence band. In the absence of thermal excitation, both insulators and semiconductors would therefore have a configuration in which the valence band is completely full and the conduction band is completely empty. Under these circumstances, neither would theoretically show any electrical conductivity.

In a metal, the highest occupied energy band is not completely full. Therefore, electrons can easily migrate throughout the material because they need to achieve only small incremental energy to be above the occupied states. In insulators or semiconductors the electron must first cross the bandgap to reach the conduction band, which reduces the amount of electrons in the highest band and so the conductivity is therefore many orders of magnitude lower compared with metals, where a small incremental energy of the electrons is enough to reach bands over the valence one. For insulators, the bandgap is usually 5 eV or more, whereas for semiconductors, the bandgap is smaller.

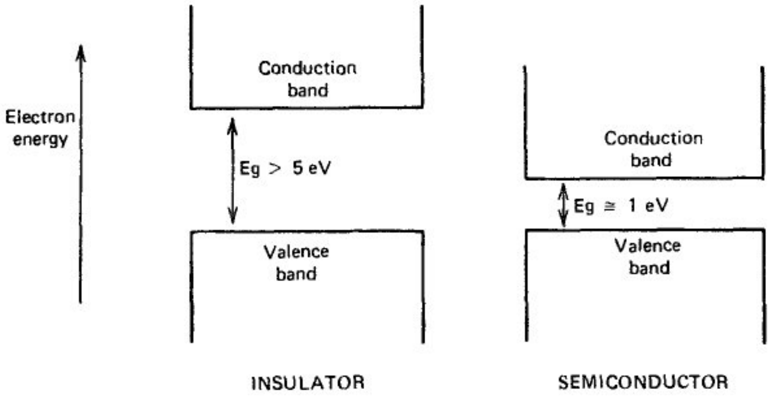

Figure 1.1: Band structure for electron energies in insulators and semiconductors.

1.1.2 Charge Carriers

At nonzero temperature, some thermal energy is shared by the electrons in the lattice. It is possible for a valence electron to gain sufficient thermal energy to be elevated across the bandgap into the conduction band. Physically, this process simply represents the excitation of an electron that is normally part of a covalent bond such that it can leave the specific bonding site and drift throughout the crystal. The excitation process not only creates an electron in the otherwise empty conduction band, but it also leaves a vacancy (called a hole) in the otherwise full valence band. The couple formed by the two is called an *electron-hole* pair. As explained in the next section, the electron in the conduction band can be made to move under the influence of an applied electric field. The hole, representing a net positive charge, will also tend to move in an electric field, but in an opposite direction respect to the electron. The motion of both of these charges contributes to the observed conductivity of the material.

The probability per unit time that an electron-hole pair is thermally generated is given by

$$p(T) = CT^{3/2}exp\left(-\frac{E_g}{2kT}\right) \tag{1.1}$$

where:

T = absolute temperature

E_g = bandgap energy

k = Boltzmann constant

C = proportionality constant characteristic of the material

As reflected in the exponential term, the probability of thermal excitation is critically dependent on the ratio of the bandgap energy to the absolute temperature. Materials with a large bandgap will have a low probability of thermal excitation and consequently will show the very low electrical conductivity characteristic of insulators. If the bandgap is as low as several electron volts, sufficient thermal excitation will cause a conductivity high enough for the material to be classified as a semiconductor. In the absence of an applied electric field, the thermally created electron-hole pairs ultimately recombine, and an equilibrium is established in which the concentration of electron-hole pairs observed at any given time is proportional to the rate of formation. From Eq. 1.1, this equilibrium concentration is a strongly dependent on temperature and will decrease drastically if the material is cooled.

1.1.3 The Action of Ionizing Radiation in Semiconductors

When a charged particle passes through a semiconductor with the band structure shown in Fig. 1.1, the overall significant effect is the production of many electron-hole pairs along the track of the particle. The production process may be either direct or indirect, in that the particle produces high-energy electrons (or delta rays) that subsequently lose their energy in producing more electron-hole pairs. Regardless of the detailed mechanisms involved, the quantity of practical interest for detector applications is the average energy expended by the primary charged particle to produce one electron-hole pair. This quantity, often called the ionization energy and given the symbol ϵ, is experimentally observed to be largely independent of the energy of the incident radiation. This important simplification leads to the interpretation of the number of electron-hole pairs produced in terms of the incident energy of the radiation, provided the particle is fully stopped within the active volume of the detector. When radiation interacts in a semiconductor, the energy deposition always leads to the creation of equal numbers of holes and electrons.

The dominant advantage of semiconductor detectors lies in the smallness of the ionization energy, it is of the order of few eV, compared with about 30 eV required to create an ion pair in typical gas-filled detectors. Thus, the number of charge carriers is 10 times greater for the semiconductor case, for a given energy deposited in the detector. The increased number of charge carriers has two beneficial effects on the attainable energy resolution. On the one hand, at low energies, the resolution may be limited by electronic noise, and the greater amount of charge per pulse leads to a better signal-to-noise ratio. On the other hand, the statistical fluctuation in the number of carriers per pulse becomes a smaller fraction of the total as the number increase. This factor often is predominant in determining the limiting energy resolution of a detector for medium to high radiation energy.

As in gas counters, the observed statistical fluctuations in semiconductors are smaller than expected if the information of the charge carriers were a Poisson process. The Poisson model would hold if all events along the track of the ionizing particle were independent and would predict that the variance in the total number of electron-hole pairs should be equal to the total number produced, or E/ϵ. The Fano factor F is introduced as an adjustment factor to relate the observed variance to the Poisson predicted variance:

$$F = \frac{\text{observed statistical variance}}{E/\epsilon} \tag{1.2}$$

For good energy resolution, one would like the Fano factor to be as small as possible.

1.1.4 Migration of Charge Carriers in an Electric Field

If an electric field is applied to the semiconductor material, both the electrons and holes will undergo a net migration. The motion will be the combination of a random thermal velocity and a net drift velocity parallel to the direction of the applied field. The motion of the conduction electrons is a relatively easy process to visualize, but the fact that holes also contribute to conductivity is less obvious. A hole moves from one position to another if an electron leaves a normal valence site to fill an existing hole. The vacancy left behind by the electron then represents the new position of the hole. Because electrons will always be drawn preferentially in an opposite direction to the electric field vector, holes move in the same direction as the electric field. This behaviour is consistent with that expected of a point positive charge, because the hole actually represents the absence of a negatively charged electron.

At low-to-moderate values of the electric field intensity, the drift velocity v is proportional to the applied field. Then a mobility μ for both electrons and holes can be defined by Eq. 1.3

and Eq. 1.4 respectively, where V/d is the ratio between the applied voltage and the detector thickness, which express the electric field magnitude.

$$v_e = \mu_e V/d \tag{1.3}$$

$$v_h = \mu_h V/d \tag{1.4}$$

1.1.5 Charge Induction

In order to construct a practical radiation detector, some means must be provided to collect the electrical charges created by the radiation at either boundary of the semiconductor material. If two ohmic contacts are fitted on opposite faces of a slab of semiconductor and connected to a detection circuit, the equilibrium charge carrier concentrations in the semiconductor will be maintained. If an electron or hole is collected at one electrode, the same carrier species is injected at the opposite electrode to maintain the equilibrium concentrations in the semiconductor.

When a particle deposits energy in a semiconductor detector, equal numbers of conduction electrons and holes are formed within a few picoseconds along the particle track. The detector configuration that is discussed ensure that an electric field is present throughout the active volume, so that both charge carriers feel electrostatic forces that cause them to drift in opposite directions. The motion of either the electrons or holes constitutes a current that will persist until those carriers reach the electrodes. The resulting currents can be represented by the plot at the top of Fig. 1.2. Since the charge collection times are no likely to be the same because of differences in drift distance and carrier mobilities, one of the two currents will persist for a longer time than the other.

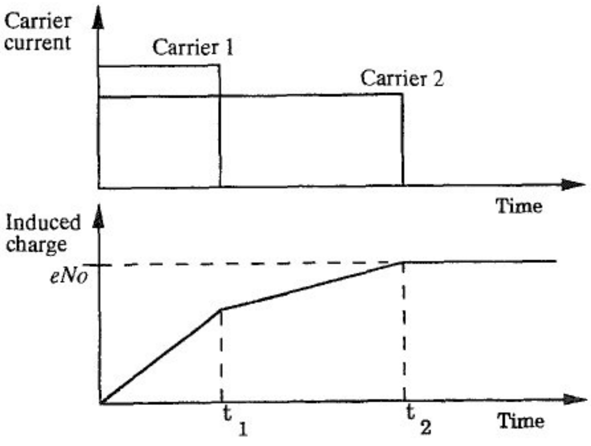

Figure 1.2: The upper plot shows an idealized representation of the electron and hole currents flowing in a semiconductor following the creation of N_0 electron-hole pairs. In the lower plot, t_1 represents the collection time for the carrier type (either electrons or holes) that is collected first, and t_2 is the collection time for the other carrier. If both are fully collected, a charge of eN_0 is induced to form the signal, where e is the electronic charge.

Signals from the detectors arise because of the motion of charge carriers after they are formed by the incident radiation. Those unfamiliar with the process sometimes have a naive (and incorrect) notion that the detector signal is formed only when the charge carriers deposit their electrical charges on the electrodes. That picture would imply a delay before the onset pulse begins to form immediately when the carriers start their motion to the electrodes. Since the pulse begins as soon as the incident particle deposits its energy in the detector, the timing of detection events can be much more accurate than if a delay were to exist. Once the last of the carriers arrives at its collecting electrode, the process of charge induction ends and the pulse is fully developed. The time evolution of the signal is of fundamental importance in understanding the timing properties of detectors as well as in predicting the effects of changes in the location of the radiation interactions on the shape of the pulse.

In order to calculate the induced charge on an electrode it is necessary to know the expression for the electric potential and the electric field. These two magnitudes are strongly dependent on the detector shape and electrodes orientation. For a rectangular detector with two plano parallel electrodes, the negative one placed at $x = 0$ and the positive one at $x = d$ and biased by a voltage V, a point-like charge q in a position $x = x_0$ induces a charge distribution $q\omega(x_0, y, z)$ on the positive contact, calculated by the method of images [1]:

$$q\omega(x_0, y, z) = \frac{q}{2\pi} \sum_{n=-\infty}^{\infty} \frac{(2n-1)d + x_0}{[((2n-1)d + x_0)^2 + y^2 + z^2]^{3/2}} \tag{1.5}$$

where y and z are the plane coordinates of the contact. The weight function $\omega(x_0, y, z)$ is the induced charge distribution on the positive contact by unit charge within the detector. The total charge induced on the full electrode (supposing a>>d where a is the side size of the electrodes) is obtained directly from 1.6 in [2], [3].

$$h'(x_0) = \frac{qx_0}{d} \tag{1.6}$$

In case of having a pixelated electrode, the total charge induced on the pixel is the integral of 1.5 over the pixel area.

$$h(x_0) = q \int_{pixel} \omega(x_0, y, z) \tag{1.7}$$

When the charge q moves from a position x_1 to a position x_2 it will induce an electric charge flow e(x_1,x_2) in the electrode only dependent on the two positions.

$$e(x_1, x_2) = h(x_2) - h(x_1) \tag{1.8}$$

For a charge drift starting in the deposition point and ending in the electrode, a current j is induced, [4].

$$j = q - h(x_0) \tag{1.9}$$

1.1.6 Trapping and Recombination

Once electrons and holes are formed in a semiconductor, they will tend to migrate either spontaneously or under the influence of an applied electric field until they are either collected at an electrode or recombination[1] takes place. There are theoretical predictions that average lifetime of charge carriers before recombination in perfectly pure semiconductors could be as large as a

---

[1] The process by which a charge carrier is captured by an impurity and is caused to annihilate.

second. In practice, lifetimes of at least three or four orders of magnitude smaller than a second that are actually observed are dominated entirely by the very low level of impurities[2] remaining on the material. Some of these impurities, such as gold, zinc, cadmium, or other metallic atoms occupying substitutional lattice positions, introduce energy levels near the middle of the forbidden gap. They are therefore classified as deep impurities (as opposed to acceptor or donor impurities that, because the corresponding energy levels lie near the edges of the forbidden band, are called shallow impurities). These deep impurities can act as traps for charge carriers in the sense that if a hole or electron is captured, it will be immobilized for a relatively long period of time. Although the trapping center ultimately may release the carrier back to the band from which it came, the time delay is often sufficiently long to prevent that carrier from contributing to the measured pulse.

In addition to impurities, structural defects within the crystal lattice can also lead to trapping and charge carrier loss. These imperfections include point defects such as vacancies or interstitials that tend to behave as acceptors or donors, respectively. Carrier loss may also occur at line defects of dislocations that may be produced in stressed crystal lattices. A dislocation represents the slippage of one crystal plane with respect to another, and its intersection with the surface of the lattice leads to a pit upon chemical etching. The density of these etched pits is often quoted as a measure of the crystalline perfection of a semiconductor sample.

Other types of deep impurities can act as recombination centers. These impurities are capable of capturing both majority and minority carriers, causing them to annihilate. An impurity level near the center of the forbidden gap might, for example, first capture a conduction electron. At a slightly later time, a hole from the valence band might also be captured, with the electron then filling the hole. The impurity site is thus returned to its original state and is capable of causing another recombination event. In most crystals, recombination through such centers is far more common than direct recombination of electrons and holes across the full bandgap.

Both trapping and recombination contribute to the loss of charge carriers and tend to reduce their average lifetime in the crystal. For the material to serve as a good radiation detector, a large fraction (preferably close to 100%) of all the carriers created by the passage of the incident radiation[3] should be collected. This condition will hold provided the collection time for the carriers is short compared with their mean lifetime. Collection times of the order of 10^{-7} s to 10^{-8} s are fairly common, so that carrier lifetimes of the order of 10^{-5} s or longer are usually sufficient

Another specification is the trapping length within the material. This quantity is simply the mean distance traveled by a carrier before trapping or recombination and is given by the product of the mean lifetime and the average drift velocity. In order to have a good detector, the trapping length should be long compared with the physical dimensions over which the charge must be collected. In the wide-bandgap semiconductors where charge trapping can be severe, it is conventional to quote the product of charge mobility and lifetime (called the "mu-tau product") to quantify the degree of charge loss. This product has units of "cm^2/V", and when multiplied by the applied electric field strength in "V/cm", results in the trapping length.

A method to evaluate the amount of trapped charge in the charge collection process is through Hecht equation (1.10) which represents the fraction of charge reaching the electrodes after the drift of the charge carriers in the detector.

$$\frac{Q*}{Q} = \frac{v_h \tau_h *}{d}\left(1 - exp\left(\frac{-x_i}{v_h \tau_h *}\right)\right) + \frac{v_e \tau_e *}{d}\left(1 - exp\left(\frac{x_i - d}{v_e \tau_e *}\right)\right) \tag{1.10}$$

---

[2] Defects of the crystal lattice created by the presence of one or more spurious atom.

[3] The ionizing radiation which interacts with the detector.

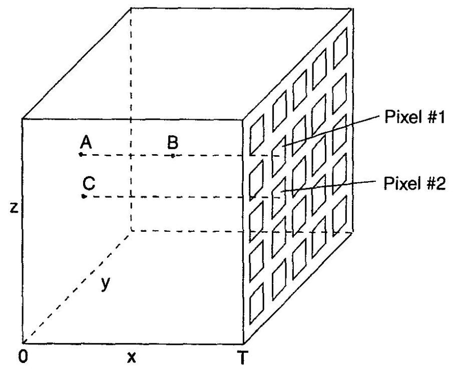

Figure 1.3: A planar detector configuration with a continuous cathode electrode on the y-z surface at the left and a pixelated anode surface on the right.

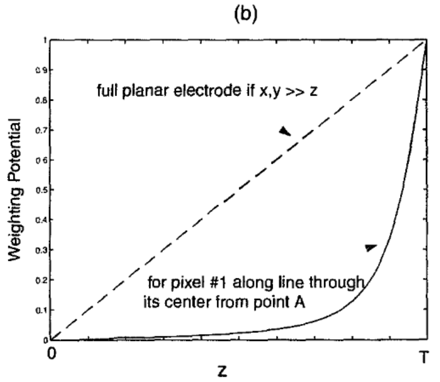

Figure 1.4: Plot of the weighting potential for a continuous anode (dashed line) and for a single pixel anode (solid line), for the case in which the pixel size is 20% of the detector thickness T.

where v is the charge carrier velocity, τ^* is the charge carrier lifetime, x_i represents the location of the radiation interaction location measured from the cathode, d is the detector width, and the e and h subscripts represent electrons and holes, respectively. As one can see, v, τ^* and d are common for all the events given that they are parameters of the system, so the amount of trapped charge given a set of conditions is only depending on the charge deposition point.

1.1.7 The Small Pixel Effect

In Fig. 1.3, the configuration of a planar detector is sketched in which the y-z surface on the left is completely covered with a conventional continuous electrode. The opposite surface has an electrode that is subdivided into a checkerboard pattern of individual pixels. Each pixel is an independent square electrode, and small gaps are present between adjacent pixels. We assume that the dimensions of the detector in the x and y directions are large compared with the thickness d, so that edge effects can be neglected in the analysis that follows.

The value of the weight function for different pixel size is shown in Fig. 1.4. Notice that the shape of the weight function is far from linear. When the relation a/d is small (small pixel), eq 1.10 takes a small value for the first time steps (x_0 turns to be x_0=vt and becomes a time variable) and increases rapidly for distances closer to the pixel electrode. Because the

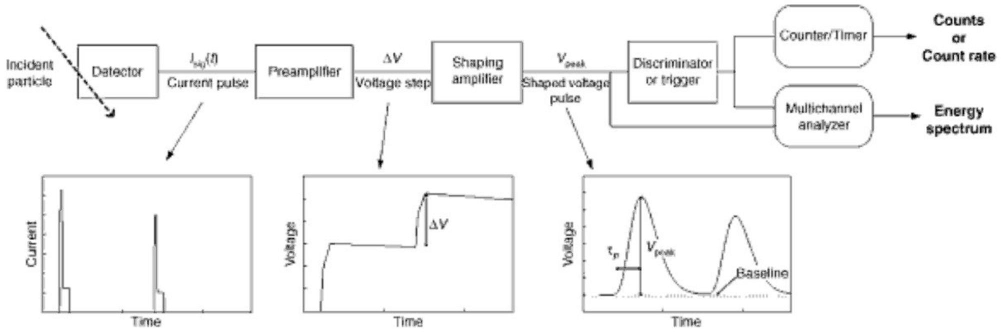

Figure 1.5: Schematic diagram of the detector and electronics. Typical outputs from each stage of the processing electronics(for two pulses) are also sketched.

induced charge is proportional to the difference in the weight function between the point of origin and collection, the electron motion will contribute much more than the motion of the positive charge for events over most of the detector volume. Only for charges created very near the pixel surface, a small fraction of the detector volume, will the positive charge motion contribute most of the charge induced on the pixel electrode. For the vast majority of events, the motion of the electron dominates the induced charge. Furthermore it is the motion close to the pixel surface that contributes most strongly to the induced charge. These consequences are often called the *small pixel effect* and are most pronounced in detectors with pixel dimensions that are small compared with the detector thickness [5]. For detectors in which electrons are much more mobile than positive charges (such as the compound semiconductors), deriving the signal from a small pixel rather than from a large-area anode can help improve energy resolution by minimizing sensitivity of the pulse amplitude to the motion of the positive charges that may not be completely collected.

1.2 Pulse Processing

The basic components on a typical signal processing chain are shown in Fig. 1.5. The components shown will be discussed in detail later, but are sketched here initially to show their overall functions. An incident quantum interacts in the detector and deposits energy that is converted into a current pulse. The total charge is usually too small to be sensed directly. The current is sent to a *preamplifier*, an interface between the detector and the subsequent electronics. The preamplifier usually has a *charge sensitive* configuration, integrating the transient current pulse to produce a voltage step ΔV proportional to Q. The *shaping amplifier* converts the preamplifier output signal into a form suitable for measurements, producing an output voltage pulse with pulse height V_{peak} proportional to the deposited charge Q. Since the size of Q reflects the energy deposited by the incident quantum in the detector, recording the pulse height distribution is a powerful method to provide information about the energy distribution of the incident radiation.

The output of the shaping amplifier should return rapidly to the *baseline* to prevent pulses from overlapping and a resulting distortion of the measurement. The output must return to true zero between pulses so that the peak is referenced to the correct baseline. The amplifier also filters high- and low-frequency noise to improve the signal-to-noise ratio. Both the noise filtering and return to baseline change the time profile or shape of the pulse, hence the name shaping amplifier.

The amplifier is characterized by a *shaping time constant* that is related to the duration of the pulse produced at its output. Since radiation interactions usually occur at random time intervals,

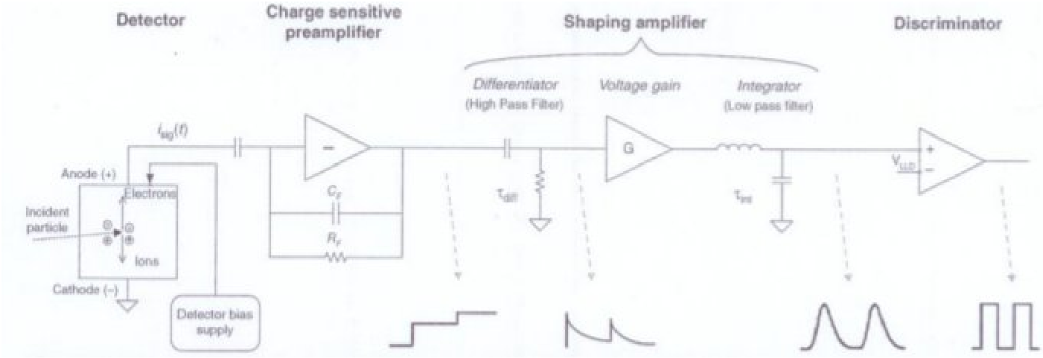

Figure 1.6: Schematic of simple signal processing electronics. This circuit is suitable for use, as shown, in many applications and is conceptually similar to more complex circuits.

there is always some probability that two pulses will overlap in time, resulting in distorted outputs. Short shaping times are desirable to minimize overlap or *pulse pile-up*. However, since a short shaping time passes more broadband electronic noise, this choice may result in a greater influence of noise on the information carried by the pulse amplitude. This tradeoff is fundamental in shaping amplifiers. Shaping amplifiers with multiple choices of shaping techniques may offer better performance in this trade space, but at the cost of more complexity, more power, and so on. Shaping amplifiers also differ in how well they maintain the baseline relative to the true zero.

The shaped pulse is sent to circuits that select pulses for further processing. This selection may be very simple -for example, an *integral discriminator*, also called a *single channel analyzer*, selects pulses with peak amplitude between upper and lower thresholds. More complex logic may reject events that pile up or exhibit distorted pulse shapes. Many systems have components that require detectors to be triggered within a narrow time interval as part of selection logic.

Selected events are then processed by circuits that produce a result that depends on the accumulation of many individual pulses over a defined measurement time. The simplest example is a counter, which counts the number of selected events over a finite time period. A more complex example is a *multichannel analyzer* or MCA. The MCA measures the pulse height for each of a series of selected events, assigning the height to one of many pulse height ranges or channels. It then increments a counter (or memory register) for the appropriate pulses that deposited energy within each of its amplitude bins. The output histogram is called the *pulse height spectrum.* It consists of digital values that can be displayed, stored, or transmitted for further processing and analysis.

Fig. 1.6 shows the schematic of a simple circuit implementing these functions. It is adequate for many systems, and even the most complex signal processing chain share many elements in common with this simple system.

1.2.1 Pulse Preamplification

For the majority of detectors, the generated charge is so small that it is impractical to deal with the signal pulses without an intermediate amplification step. The first elements in a signal-processing chain is therefore often a *preamplifier* ("or preamp") provided as an interface between the detector and the pulse-processing and analysis electronics that follow.

The preamplifier is usually located as close as possible to the detector. From a signal-to-noise standpoint, it is always preferable to minimize the capacitive loading on the preamp, and therefore long interconnecting cables between the detector and preamp should be avoided if

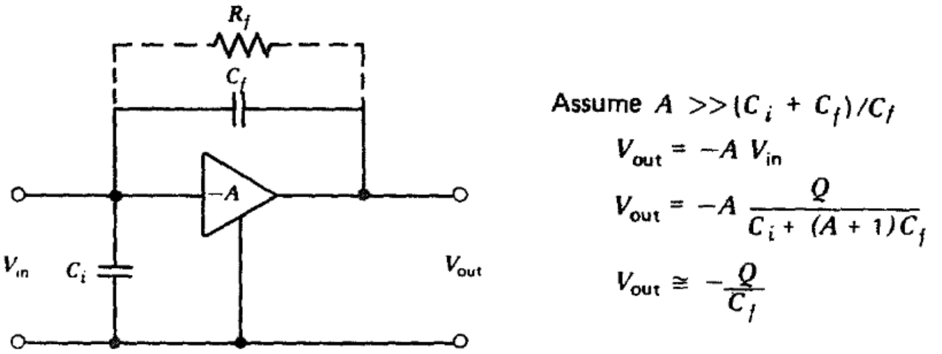

Figure 1.7: Simplified diagram of a charge-sensitive preamplifier configuration. If the conditions indicated are met, the output pulse amplitude becomes independent of the input capacitance C_i. The time constant given by the product $R_f C_f$ determines the decay rate of the tail of the output pulse.

possible. One function of the preamp is to terminate the capacitance quickly and therefore to maximize the signal-to-noise ratio. Because of convenience or safety considerations, the components that follow in the pulse processing chain often are located at some distance from the detector and preamp. Thus another requirement is for the preamp output stage to be capable of driving its signal into the large capacitance represented by the long interconnecting cable, or that it has a low output impedance.

The preamplifier conventionally provides no pulse shaping, and its output is a linear tail pulse. The rise time of the output pulse is kept as short as possible, consistent with the charge collection time in the detector itself. The decay time of the pulse is made quite large (typically 50 or 100 μs) so that full collection of the charge from detectors with widely differing collection times can occur before significant decay of the pulse sets in. Possible effects of a too fast decay time are discusses in section 3.4.

Preamplifiers can be of either the *voltage-sensitive* or the *charge-sensitive* type. In semiconductor diode detectors, the detector capacitance may change with operating parameters, in these situations, a voltage-sensitive preamp is undesirable because its response is also affected, so charge sensitive preamplifiers are the ones used with these detectors.

Charge Sensitive Preamplifier

The elements of a charge-sensitive configuration are shown in Fig. 1.7. For this circuit, the output voltage is proportional to the total integrated charge in the pulse provided to the input terminals, as long as the duration of the input pulse is short compared with the time constant $R_f C_f$. Changes in the input capacitance no longer have an appreciable effect on the output voltage. Although originally developed for use with semiconductor diode detectors, this charge-sensitive configuration has proved its superiority in a number of other applications, so that preamplifiers used with other detectors in which the capacitance does not necessarily change are also often of the charge-sensitive design.

1.2.2 Pulse Shaping

In dealing with signal pulses from radiation detectors, it is often desirable to change the shape of the pulse in some predetermined fashion. By far the most common application is in processing

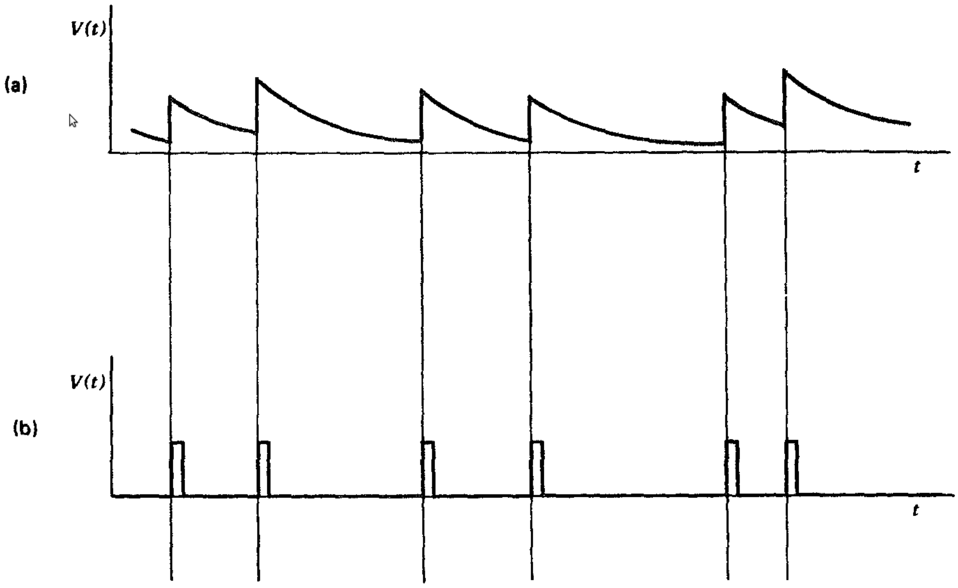

Figure 1.8: The pulses with long tails shown in part (a) illustrate the apparent variation in amplitude due to pulse pile-up. These effects can be greatly reduced by shaping the pulses as in part (b).

a train of pulses produced by a preamplifier. In order to ensure that complete charge collection occurs, preamplifiers are normally adjusted to provide a decay time for the pulse, which is quite long (typically 50 or 100 μs). If the rate of interaction in the detector is not small, these pulses will tend to overlap one another and give rise to a pulse train that has the appearance shown in Fig. 1.8a. Because it is the amplitude that carries the basic information (the charge Q deposited in the detector), the "pile-up" of pulses on the tails of preceding pulses, which have not fully decayed to zero, can be a serious problem. Because the time spacing between nuclear pulses is random, each pulse can be superimposed on a different residual tail and the resulting amplitude no longer is a good measure of A from that event.

The ideal solution is to *shape* the pulses in such a way as to produce a pulse train similar to that shown in Fig. 1.8b. Here all the long tails have been eliminated, but the information carried by the maximum amplitude of the pulse has been preserved. The pulses have been shaped in the sense that their total length has been reduced drastically but in a way that does not affect the proportionality of its amplitude to the charge Q.

CR and RC Shaping

In general electrical circuits, the term RC *shaping* refers to the use of passive resistor-capacitor networks to carry out a desired alteration in pulse shape. When discussing nuclear pulse shaping, it is conventional to make a semantic distinction between *differentiator* or CR networks on one hand, and *integrator* or RC networks on the other. Both operations can also be thought of as filtering in the frequency domain, and one purpose of pulse shaping is to improve the signal-to-noise ratio by limiting the response of the instrumentation to those frequency ranges in which the signal has useful components, while reducing as much as possible the transmission of frequency components from the various sources of noise.

The different responses of the CR and RC shapers for a step function input are shown in Fig. 1.9 and Fig. 1.10. In both types of network, the *time constant* given by the product of

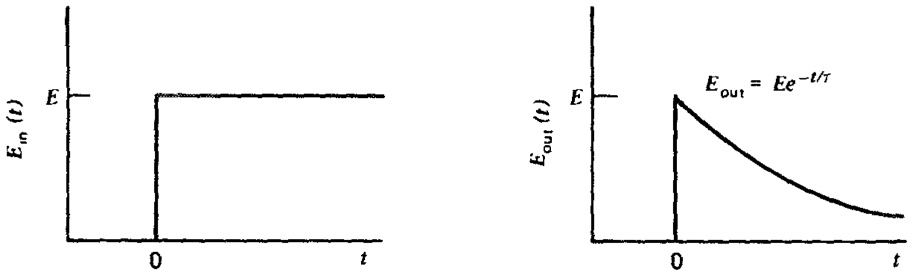

Figure 1.9: A high-pass CR filter or differentiator network. The response to a step function input is illustrated.

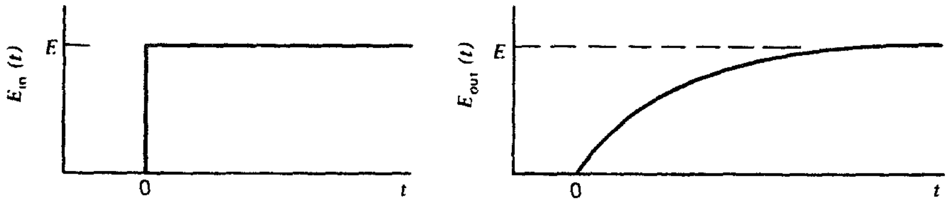

Figure 1.10: A low-pass RC filer or integrator network. The response to a step function input is illustrated.

resistance and capacitance plays a critical role. In the analysis that follows, we represent this time constant as τ:

$$\tau \equiv RC \tag{1.11}$$

The units of τ are seconds and R is in ohms and C is in farads.

CR-RC Shaping

The output of a single differentiating network shown in Fig. 1.9 is not a very attractive waveform for pulse analysis systems. The sharply pointed top makes subsequent pulse height analysis difficult because the maximum pulse amplitude is maintained only for a very short time period. Furthermore, because the differentiation allows all high-frequency components of any noise mixed with the signal to be passed by the network, the signal-to-noise characteristics of the network in practical applications of these drawbacks are considerably improved. The combination of a single stage of differentiation followed by a single stage of integration is in fact one method of shaping preamplifier pulses.

Fig. 1.11 shows the elements of the basic CR-RC shaping network. An ideal unity-gain operational amplifier (with infinite input impedance and zero output impedance) separates the two individual networks for impedance isolation so that neither network influences the operation of the other. The general solution of the response of the combined network to a step voltage of amplitude E at t=0 is shown in 1.12

$$E_{out} = \frac{E\tau_1}{\tau_1 - \tau_2}\left(e^{-t/\tau_1} - e^{-t/\tau_2}\right) \tag{1.12}$$

where τ_1 and τ_2 are time constants of the differentiating and integrating networks, respectively. Plots of this response for several different combinations of τ_1 and τ_2 are shown in Fig. 1.12.

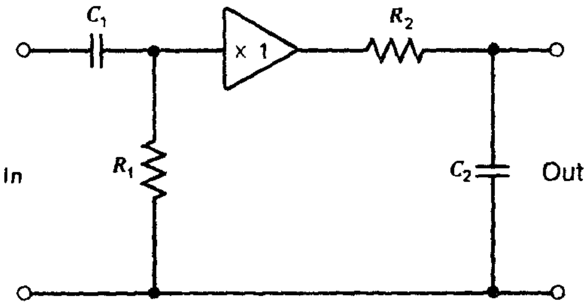

Figure 1.11: A shaping network consisting of sequential differentiating and integrating stages, sometimes denoted a CR-RC network.

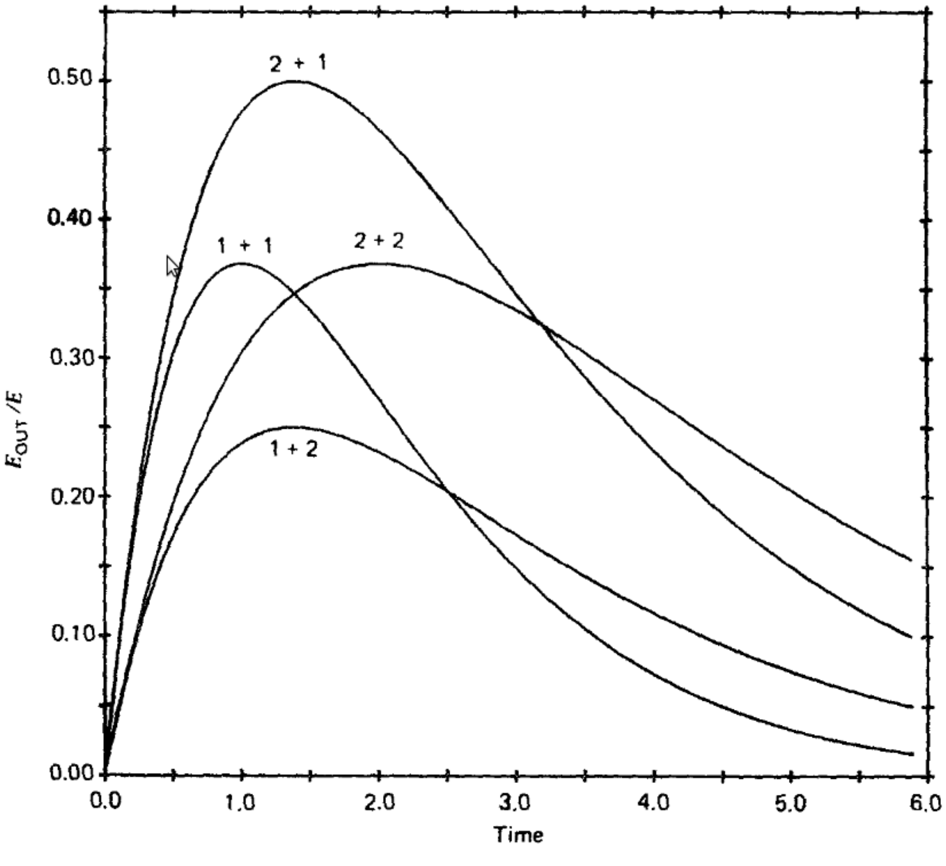

Figure 1.12: The response of a CR-RC network to a step voltage input of amplitude E at time zero. Curves are shown for four pairs of differentiator + integrator time constants. Units of the time constants and time scale are identical.

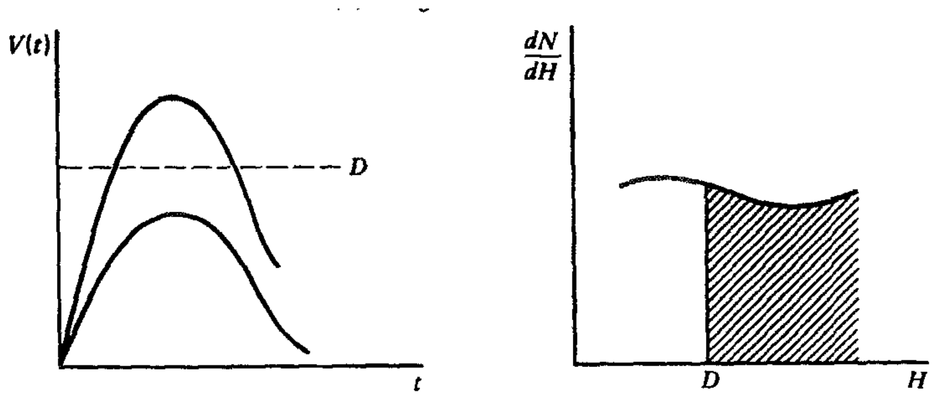

Figure 1.13: The function of an integral discriminator. Of the two input pulses shown, only the larger clears the discriminator level D and produces a logic pulse output. The effect is to select only the area to the right of the amplitude D in the differential pulse height spectrum.

One factor in the choice for the time constant of the shaping circuits is the charge collection time in the detector being used. In the interests of reducing pile-up, one would like to keep these time constants short so that the shaped waveform can return to the baseline as quickly as possible. On the other hand, once the shaping time constant becomes comparable with the rise time of the pulse from the preamplifier, the input to the network no longer appears as a step voltage and some of its amplitude is lost. This loss is called the *ballistic deficit* and can be avoided only by keeping the time constants long compared with the charge collection time in the detector. At the same time, the signal-to-noise characteristics of the pulses are also influenced by the choice of shaping time. The proper choice for shaping time for a given circumstance thus becomes a complex balance between factors involving ballistic deficit, electronic noise, and pulse pile-up.

1.2.3 Signal Discrimination

In order to count the pulses reliably, the shaped linear pulses must be converted into logic pulses. The *integral discriminator* is the simplest unit that can be used for this conversion an consists of a device that produces a logic output pulse only if the linear input pulse amplitude exceeds a set discrimination level or also called *threshold*. If the pulse amplitude is below the discrimination level, no output appears. This selection process is illustrated in Fig. 1.13.

The threshold is normally adjustable by a front-panel control. In many counting situations, the level is set just above the system noise so that the maximum sensitivity for counting detectors pulses of all sizes is realized. Other situations may call for a higher discrimination level to count selectively only events above a set minimum size. For example, much of the background may be limited to relatively low pulse amplitudes so that some finite discrimination level may greatly enhance the signal-to-background counting ratio.

1.3 Detector Signal Analysis

A measurement of the differential pulse height spectrum from a radiation detector can yield important information on the nature of the incident radiation or the behaviour of the detector itself and is therefore one of the most important functions to be performed in nuclear measurements. By definition, the differential pulse height spectrum is a continuous curve that plots the value of dN/dH (the differential number of pulses observed within a differential increment of pulse height

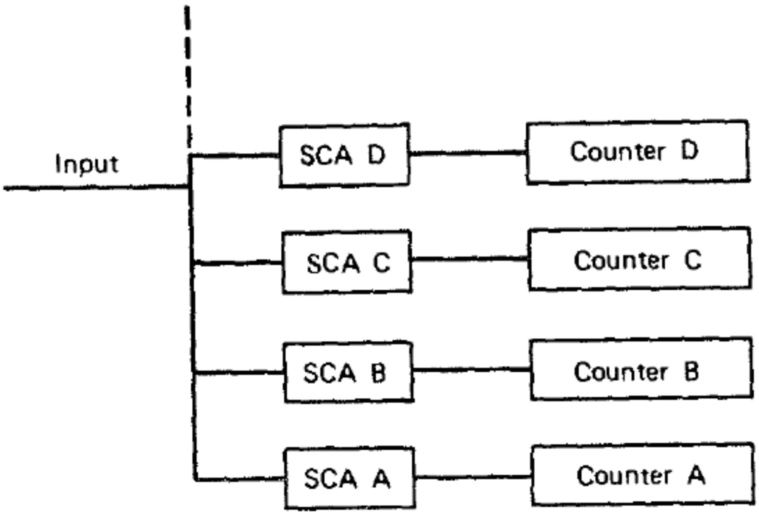

Figure 1.14: An array of stacked single-channel analyzers. Windows A, B, C, ... are assumed to be contiguous and of equal width ΔH, with A at the bottom of the pulse height scale.

H) versus the value of the pulse height H. The ratio of the differentials can never be measured exactly, but rather all measurement techniques involve a determination of ΔN/ΔH (the discrete number of pulses observed in a small but finite increment of pulse height H). The increment in pulse height ΔH is commonly called the *window width* or *channel width.* Provided ΔH is small enough, a plot of ΔN/ΔH versus H is a good discrete approximation to the continuous curve that represents the actual differential pulse height spectrum. As a practical matter, a distinction is seldom made between the continuous distribution and its discrete approximation, and all such plots are generally referred to as differential pulse height distributions or *pulse height spectra.*

1.3.1 Single-Channel Methods

The differential discriminator (single-channel analyzer [SCA]) can be used to record a steady-state pulse height spectrum. The window is set to a small width ΔH and the number of output pulses produced over a measurement period is recorded as ΔN. In a somewhat tedious process, this window can then be moved stepwise over the pulse height range of interest. Sequential measurements of ΔN/ΔH plotted at the midpoint H value of the window will then trace out the shape of the differential distribution. This serial process is inefficient, in that most pulses are ignored during a given measurement since they lie outside the specific window chosen. However, before the days of the multichannel analyzers, this manual procedure was often the only method available to measure pulse height spectra.

A better approach is to employ multiple SCAs as in Fig. 1.14. Here the measurement is converted from one that is serial to one that is parallel, and every pulse can now contribute to the measured spectrum. All the inputs are connected together and each output fed to a separate counter. The lower level of the SCA at the bottom of the stack is set to zero, and that for the top SCA is set to correspond to the largest pulse height of interest. The lower level of the intermediate SCAs are arranged at equal to the spacing between these extremes. The window width of each SCA is identical and is set equal intervals between adjacent discrimination levels. This arrangement thus provides a series of contiguous pulse height windows of equal width, as illustrated if Fig. 1.15.

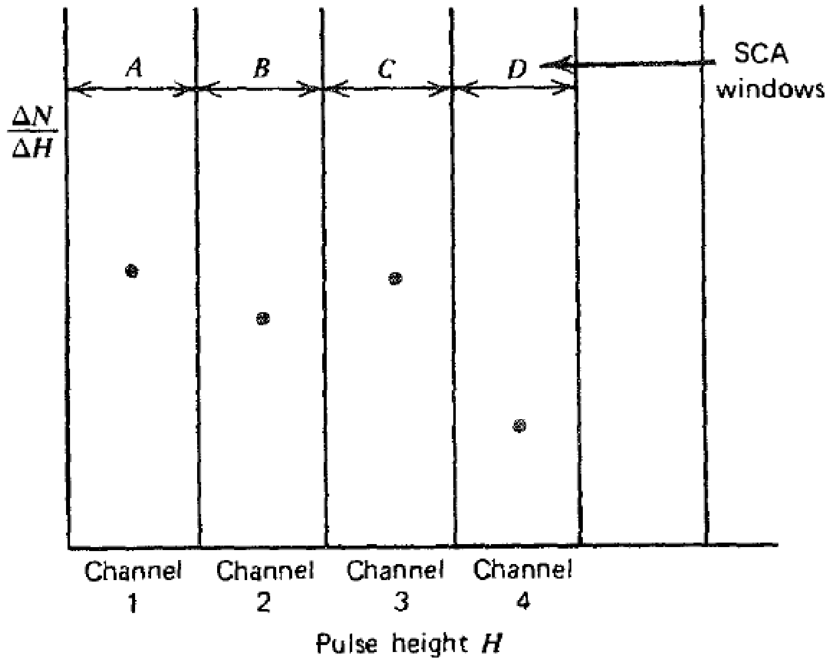

Figure 1.15: A point-wise representation of the differential pulse height distribution obtained from the stacked SCA array of Fig. 1.14 by plotting the content of each counter ΔN (normalized to the window width ΔH) versus the midpoint of the corresponding SCA window.

An input pulse presented to this array will fall into one and only one of the multiple windows set by the SCAs. Therefore, each input pulse results in an increment of one count added to the corresponding SCA counter. One can therefore view the overall process as the sorting of each input pulse into the proper window and incrementing the content of that counter by one. A small pulse will correspond to a window near the bottom of the stack, whereas a large pulse will fall into a window near the top. At the end of a measurement period, the sum of all the counters will simply be the total number of pulses presented to the input.

If we now plot the number of recorded pulses ΔN in each counter divided by the window width ΔH versus the average pulse height for each window, we derive a discrete representation of the differential pulse height distribution. In this context, each window is conventionally called a *channel* and is numbered in increasing order from left to right. The lowest channel corresponds to the pulse height window at the bottom of the range and records only those pulses whose amplitudes are very small. The largest channel numbers are plotted at the right of the horizontal axis and record only the pulses of largest amplitudes.

This process of sorting successive signal pulses into parallel amplitude channels is commonly called a *multichannel pulse height analysis.* As a practical matter, schemes based on stacked independent SCAs are seldom attractive because of complications introduced by drifts int the various discrimination levels and window widths. These drifts can lead to overlapping or non-contiguous channels whose width may also not be constant. As a result, other approaches have evolved for accomplishing the same purpose. The standard device designed to carry out this function is known as a *multichannel analyzer* (MCA).

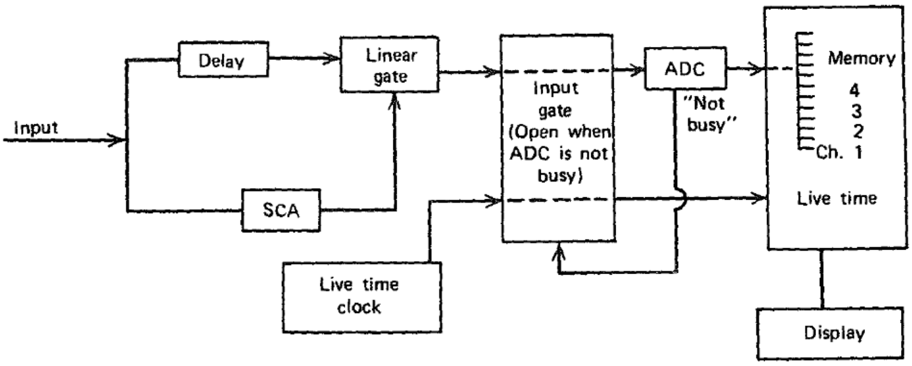

Figure 1.16: Functional block diagram of a typical MCA based on analog pulse processing.

1.3.2 The Multichannel Analyser

The multichannel analyzer (MCA) operation is based on the principle of converting an analog signal (the pulse amplitude) to an equivalent digital number. Once this conversion has been accomplished, the extensive technology available for the storage and display of digital information can be brought to bear on the objective of recording pulse height spectra. As a result, the analog-to-digital converter (ADC) is a key element in determining the performance characteristics of the analyzer. The basic configuration of a MCA depends on the detector pulse processing technique employed for pulse shaping, which can be either analog or digital pulse shaping. The analog pulse shapers produce analog pulses, which are supplied to the MCA. Thus, the MCA must incorporate an ADC to convert the pulse peak amplitude into a digital value. Digital pulse shapers themselves utilize fast ADCs and operate with digital (discrete) signals. Therefore, the MCA in this case does not need an additional ADC.

MCA Based on Analog Pulse Processing

The multichannel analyzer for analog pulse processing systems is comprised of the basic components illustrated in Fig. 1.16. The flash and subranging ADCs used in digital pulse processing produce a continuous series of digital output values at a fixed clock frequency. In contrast, the ADCs intended for use in MCAs based on analog pulse shaping operate in a different mode. They are designed to produce only a single output value for each pulse presented to their input that is proportional to the peak amplitude of that pulse. They are therefore often called *peak sensing ADCs* or *spectroscopy ADCs*. The input circuitry for these ADCs must include a capability to sense the arrival of an input pulse and to sample and hold the maximum amplitude of that pulse for a time needed to carry out the conversion to a digital value. The output of the ADC is then provided to a register that is used to address and increment a standard digital memory.

As illustrated in Fig. 1.16, an *input gate* is usually provided to block pulses from reaching the ADC during the time it is "busy" digitizing a previous pulse. The ADC provides a logic signal level that holds the input gate open during the time it is not occupied. Because the ADC can be relatively slow, high counting rates will result in situations in which the input gate is closed for much of the time. Therefore, some fraction of the input pulses will be lost during this dead time, and any attempt to measure quantitatively the number of pulses presented to the analyzer must take into account those lost during the dead time.

To help remedy this problem, most MCAs provide an internal clock whose output pulses are routed through the same input gate and are stored in a special memory location. The clock output is a train of regular pulses synchronised with an internal crustal oscillator. If the fraction of time the analyzer is dead is not excessively high, then it can be argued that the fraction of clock pulses that is lost by being blocked by the input gate is the same as the fraction of signal pulses that is lost by being blocked by the input gate is the same as the fraction of signal pulses blocked by the same input gate. Therefore, the number of clock pulses accumulated is a measure of the *live time* of the analyzer or the time over which the input gate was held open. Absolute measurements therefore can be based on a present value of live time, which eliminates the need for an explicit dead time correction of the data.

1.4 Semiconductor Detector for Positron Emission Tomography

Studies of semiconductor detectors for medical applications have increased in the last decade. In particular, CdTe and CdZnTe show optimal properties that make them very good candidates to lead a new generation of nuclear medicine imaging devices. The features of this kind of detectors and their advantages compared to the crystal-PMT or crystal-APD used nowadays will be shown in this section.

1.4.1 Basics Principles of PET

Positron emission tomography (PET) is a nuclear medicine imaging technique that produces a three-dimensional image or picture of functional processes in the body. The system detects pairs of gamma rays emitted indirectly by a positron-emitting radionuclide (tracer), which is introduced into the body on a biologically active molecule. Three-dimensional images of tracer concentration within the body are then constructed by computer analysis. In modern scanners, three dimensional imaging is often accomplished with the aid of a CT X-ray scan performed on the patient during the same session, in the same machine.

PET is based on the principle of the coincidence detection of the two 511 keV photons arising from positron emitters (through proton β^+ decay, see eq 1.4.1) in opposite directions (Fig. 1.17a) [6]. In general, a PET scanner utilizes a ring of detectors that surround the patient, and has special circuitry that is capable of identifying the photon pairs produced during annihilation (Fig. 1.17b).

$$p \rightarrow n + \beta^+ + \nu_e \tag{1.13}$$

p: proton
n: neutron
β^+: positron
ν_e: electron neutrino

Positron emitters such as ^{18}F are used to label substrates such as deoxyglucose (DG) (Fig. 1.17c) to create the radiopharmaceutical FDG. The radioactive PET agent is then transported by the blood circulation and incorporated into the organ of interest through the metabolism of the pharmaceutical, see tab 1.1. For FDG, the relevant metabolic process is glucose utilization. FDG has become the most widespread radiopharmaceutical for PET studies due to the sort range positrons emitted, the relatively long lifetime, and because the increased uptake of glucose by tumor cells is a very well known process [7]. The radiopharmaceutical is first injected into the patient, and the patient is then positioned in the PET scanner (Fig. 1.17d). When a

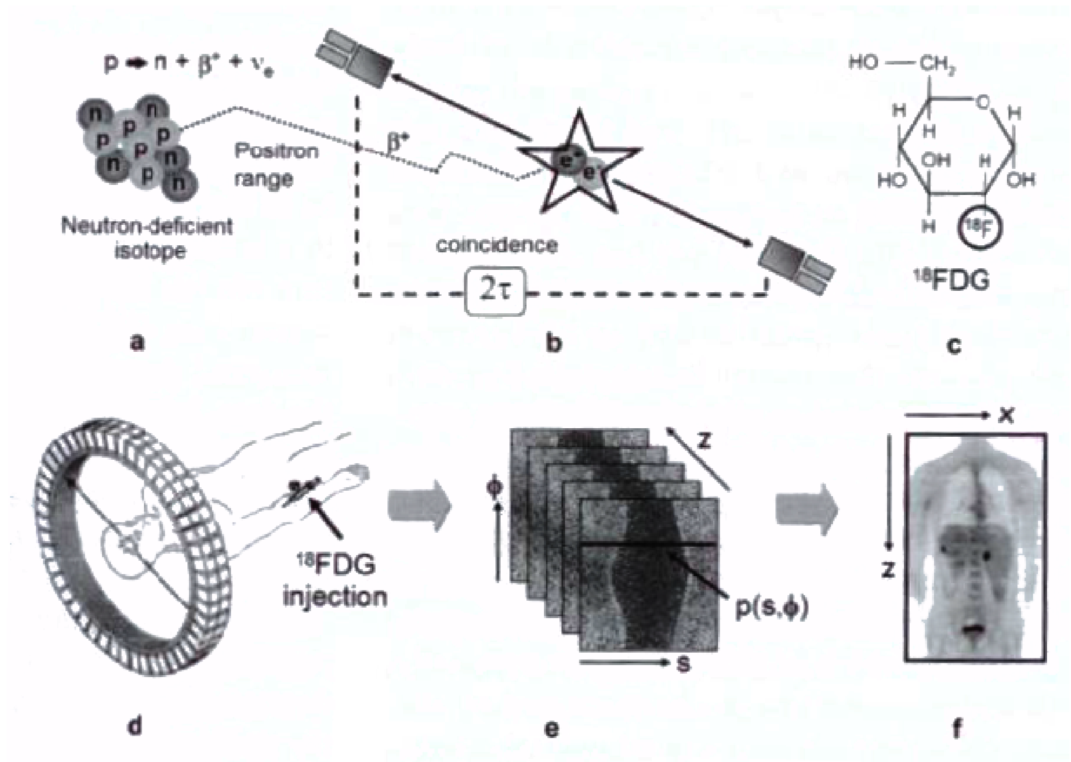

Figure 1.17: Physical principles of PET imaging. a) the decay of a proton rich isotope; b) the detection in coincidence of two photons from the e^+e^- annihilation; c) FDG radiopharmaceutical; d) the injection of FDG and the detection in coincidence of annihilation photons by a PET scanner; e) the collection of the detected events into sinograms; f) the coronal view of the final reconstructed whole-body image that is a map of glucose uptake.

photon pair from positron annihilation is detected in coincidence by two opposite detectors of the scanner, it is known that the annihilation (and thus the decay event) took place somewhere along a straight line, called line of response (LOR), between those two detectors. This information is stored in special matrices, called sinograms, where each row in the matrix represents a parallel projection, $p_z(s,\Phi)$, of the activity distribution in the patient at a specific angle (Φ) and axial position (z) (Fig. 1.17e); s is the radial coordinate within a given parallel projection. The sinograms are used to mathematically compute the three-dimensional distribution of the positron emitter, resulting in a series of tomographic emission images. The images shown in Fig. 1.17f are maps of FDG accumulation throughout the body reflecting glucose utilization by the different tissues.

Radionuclide	Half-life (min)	Substrate	Application
^{11}C	20.4	^{11}C-methionine	detect tumors with high rates of protein synthesis
^{13}N	10	^{13}N-ammonia	cardiac blood flow studies
^{15}O	2	^{15}O-water	blood flow studies
^{18}F	110	^{18}F-FDG	glucose metabolism tracer

Table 1.1: Properties of common positron emitters and their applications [8].

1.4.2 Requirements of a Detector to be used in PET

The following features make a detector to be suitable for use in PET.

Adequate Depth of Interaction

One of the constant goals in nuclear medicine is to increase the detection efficiency in order to reduce the dose needed to be applied to the patient. The detector should have a depth of interaction such that an important fraction of the photons are stopped in a few centimeters of the material.

Excellent Energy Resolution

One of the key points in the image reconstruction method is to be able to identify if the detected photon has interacted with the detector either by photoelectric or Compton interaction. A good energy resolution allows one to do it and only keep the photoelectric 511 keV photons, which determine the most precise LORs.

Excellent Spatial Resolution

Regardless of how the photon interacts with the detector (photoelectric or Compton process) it is always important to have a good spatial resolution of the interaction point in order to reconstruct LORs with much precision.

Good Coincidence Time Resolution

The wider the coincidence time window is the more probability to have a multiple coincidence (more than 2 detections) and so to loose this information. An increase of the multiple coincidences will lead to a decrease of the efficiency. In semiconductor detectors this is a crucial point due to the slow pulse formation compared to crystal-PMT detectors.

Immune to High Magnetic Fields

Just for simultaneous PET-MRI scanners. Magnetic fields should not affect the performance of the detector given that the MRI scanner can create up to 4.5 T ones.

1.4.3 State-of-the-art PET Scanners

The state-of-the-art detectors for PET are based on LSO crystals that are usually made of 4 mm x 4 mm x 10 mm coupled to PMT, APD, or similar photon-sensitive device. The light yield of LSO for 511keV gamma is about 4000 phe. At best, the FWHM that can be achieved with LSO at 511keV is around 6%. This intrinsic limitation in the energy resolution restricts the ability to remove scattered events which are a significant noise contamination to the reconstructed image. The typical length (in the radial direction) of the LSO crystals is about 10 mm, which implies a significant uncertainty of the impact point in the radial direction and induces an error in the projection of the LOR. This error deteriorates the quality of the reconstructed image.

1.4.4 CdTe Detectors for PET Scanners

Tab. 1.2 sketches the main properties of the most used materials as semiconductor detectors. The three of them achieve a very good energy resolution given that they are semiconductors, however, CdTe has the biggest bandgap so it performs better at room temperature and has also

Material	Density(g/cm^3)	Bandgap (eV)	Attenuation Coefficient for 500 keV (cm^2/g)
Si(300 K)	2.33	1.12	$8.748 \cdot 10^{-2}$
Ge(300 K)	5.33	0.67	$8.212 \cdot 10^{-2}$
CdTe(300 K)	6.06	1.52	$9.291 \cdot 10^{-2}$

Table 1.2: Properties of Semiconductor Materials

the biggest attenuation coefficient, which is clearly better for the depth of interaction problem. These two points are sufficient to determine the CdTe an excellent candidate for this purpose.

Pixelated CdTe detectors used in the novel PET design shown in [9] can meet all the requirements previously mentioned:

- Arbitrarily increment the depth of absorption in order to achieve high detection efficiency for 511 keV photon.
- Improve the scattered event rejection due to the excellent energy resolution (down to 1% for 511 keV) and obtain a better signal-to-noise ratio.
- Improve the spatial resolution by segmenting the CdTe into millimeter-size pixels (or voxels), something that it is not possible to achieve with scintillating crystals.
- Operate under strong magnetic fields given that the orientation of the electric field on the sensor would be parallel to an hypothetical magnetic field generated by an MRI scanner.
- Increase of the detection efficiency due to the absence of cracks in the scanner due the trapezoidal shape of the modules [9].
- Construct either a trapezoidal parallelepiped or rectangular parallelepiped shaped module to obtain a full planar or cylindrical geometry and so use the detector for different medical imaging purposes.

Chapter 2

Characterization of the CdTe Detector

2.1 Experimental Setup

The setup has been designed to measure the coincidence time resolution and energy resolution of a CdTe detector. Two equal detectors have been placed in a back-to-back configuration with radioactive source between them (see Fig. 2.1). Each detector is placed together with the signal processing electronics in an aluminum box of 220 mm × 145 mm × 105 mm size together. The detector consists of a CdTe Schottky diode with dimensions 4 mm x 4 mm x 2 mm, developed by ACRORAD. The detector anode is made of Au/Ti/Al and the cathode made of Pt.

The bias voltages are applied with two Hivolt power supplies model J4-3N, which delivers -330 V output per 1 V input. They are fed with a Keithley 2410 high voltage SourceMeter which at the same time is controlled by the DAQ software application. In order to avoid polarization effects, the bias voltage is temporally ramped down and kept at 0 V for 30 s before being ramped up again, this process is repeated every 15 min.

Both detectors are kept inside a fridge at -8°C. Nitrogen gas has been continuously fluxed into the two boxes in order to keep humidity below 20% and avoid condensation (Dew Point at -8°C and 20% humidity is -27°C).

The block diagram of the detector electronics is depicted in Fig. 2.2. Each diode output pulse is integrated with an AMPTEK charge sensitive preamplifier A250 which is mounted on the AMPTEK pc250 board. For 511 keV depositions on the diode, the output signal of the preamplifier is approximately 18 mV, what leads to a gain of 35 mV/MeV. The signal is divided into two, one of them is amplified by a factor 2 to improve the shaping precision and the other one is amplified by a factor 9 to perform a better discrimination of the signal. The 2-gain signal is connected to an AMPTEK pc275, a 5-pole shaper based on the pulse amplifier A275 which converts the output pulse into an almost Gaussian shape with amplitude proportional to the deposited charge on the detector. The peak sensing VME module CAEN 785N measures the maximum of the signal within a 4 μs time window provided by the pulse generator, which is generated by the coincidence trigger described later. The CAEN 785N module is controlled by the DAQ software developed within Labview environment. The 9-gain amplifier branch is connected to a LeCroy 821 quad discriminator, with the threshold set at around 8 mV, which is the equivalent for a 25 keV deposition on the detector.

The block diagram of the setup for coincidence time measurements is shown in Fig. 2.3. In order to measure the time difference between coincident signals coming from the two detectors, a time to digital converter (TDC) module has been used. It is triggered by an AND logic module to recognize events belonging to the same annihilation. This AND logic between the two signals

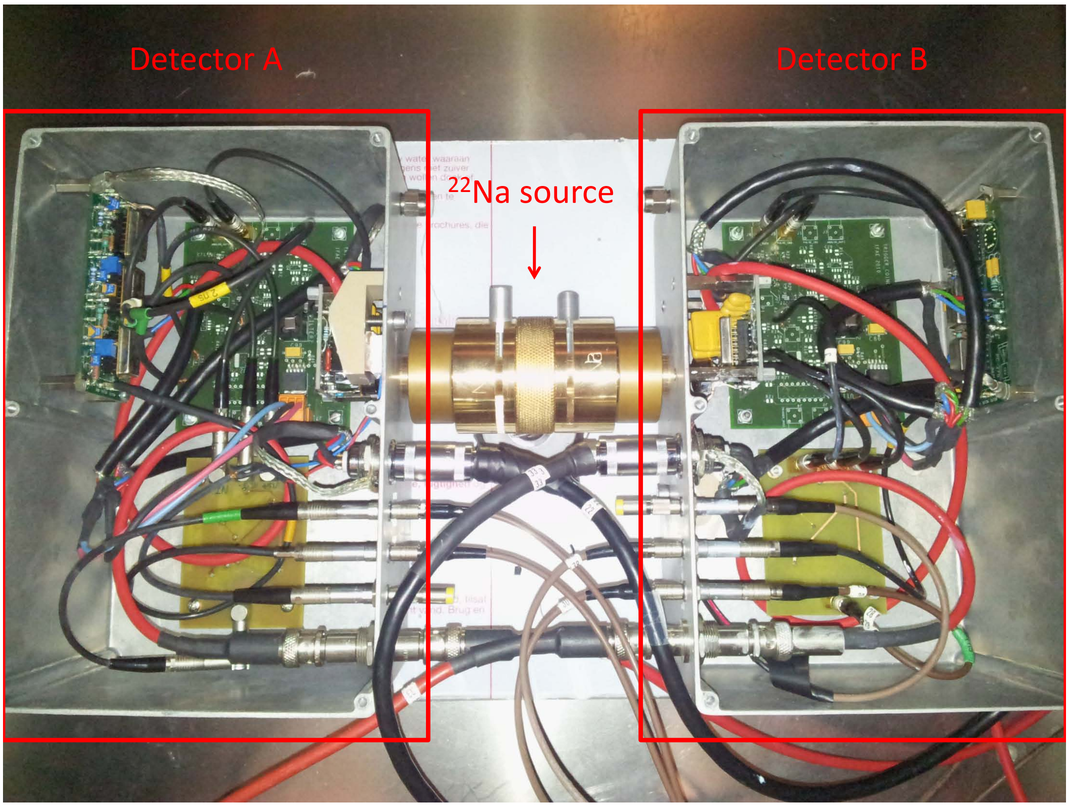

Figure 2.1: Experimental setup consisting of two CdTe detectors with a radioactive source placed in the middle

enables the TDC and gates the CAEN 785 for 4 μs. The remaining outputs of the discriminators are delayed 250 ns before being fed into the TDC for the time difference measurement. All the devices including the CAEN modules and the high voltage power supplies are controlled by the DAQ Labview application. For each coincidence, three magnitudes are taken: the time difference $\Delta t = t_a - t_b$, the detector A energy, E_a, and the detector B energy, E_b.

2.2 Experimental Strategy

The whole DAQ software has been developed as a Labview application. This software controls all the devices involved in the setup so the process is completely automatized. The ROOT framework [10] has been employed for the analysis of the output data. ROOT is a C++ based environment developed specially for data analysis processes in high energy physics and it allows to handle and analyse huge amounts of data.

For the measurements of mobility of electrons and holes, the output signal of the preamplifier has been taken with the oscilloscope. This output consists of a X-Y set of points that can be plotted to obtain the curve of the signal. The *TGraph* class of ROOT has been used for this purpose and some linear fits have been applied on it to measure the slope of the curve and, consequently, the velocity.

For the energy resolution measurements several spectroscopies with different isotopes, ^{22}Na and ^{57}Co, have been obtained. The output of the peak sensing module is the maximum value of the input signal coming from the output of the AMPTEK pc275 measured within a certain

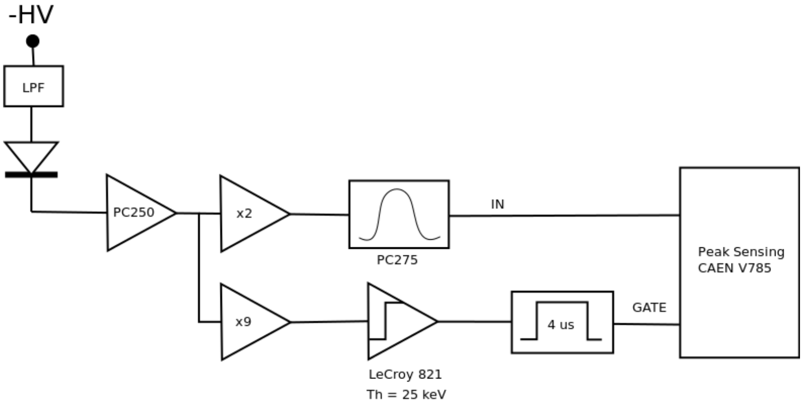

Figure 2.2: Part of the electronic circuit used to measure the energy.

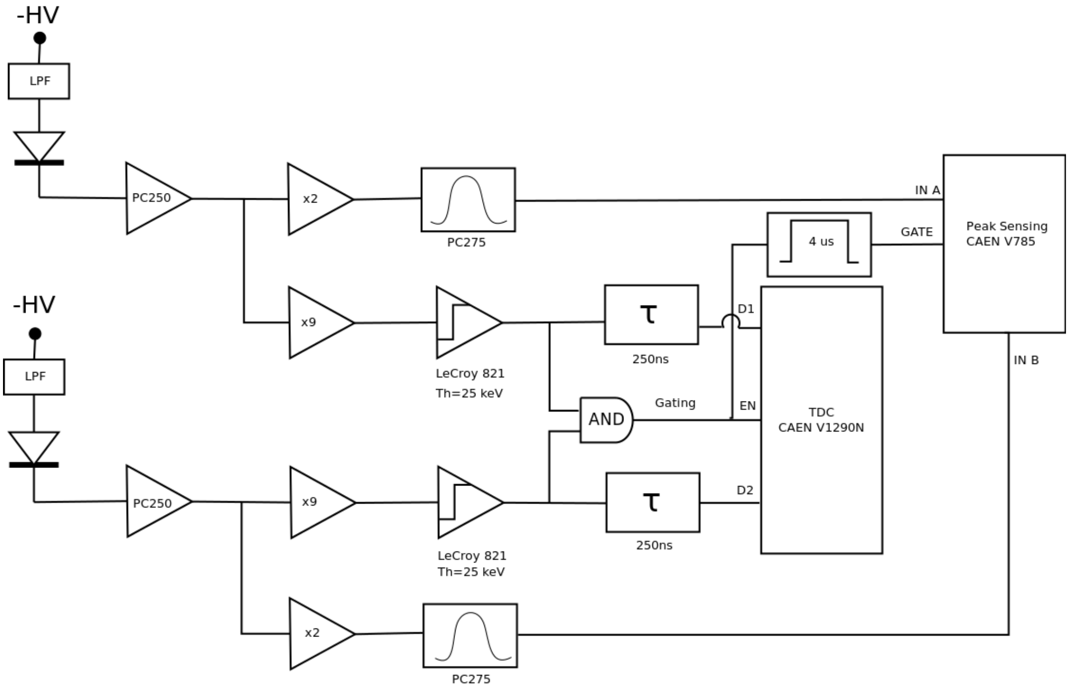

Figure 2.3: Scheme of the electronic circuit used to measure the time difference between the two signals of response of the two CdTe detectors.

time window defined by an arbitrary gate pulse. For each spectroscopy the full set of amplitudes from the peak sensing module is transformed from ADC counts into the corresponding energy distribution by a two step calibration. At first, the energy offset is calculated by measuring the pedestal noise; second, a global scale factor is applied in order to position the main photo peak in correspondence of the expected energy (511 keV for ^{22}Na and 122 keV for ^{57}Co).

In order to measure the pedestal noise, a set of random triggered data has been taken before each measurement. Pedestals are expected to follow a normal distribution because mostly due to electronic (white) noise. A Gaussian fit has been applied on the data to obtain the mean value of the distribution. This value is the one that has been subtracted to the real data. A picture with an example of a noise distribution with a Gaussian fit is shown in Fig. 2.4. The sigma of this fit is a good measure of the intrinsic noise of the setup.

As explained, the final calibration factor from ADC counts to keV is obtained with the simple procedure of forcing the main photo-peak position. For example, in the case of the ^{22}Na source, after the pedestal subtraction, a Gaussian fit has been applied to the 511 keV peak. The scale factor is calculated as the ratio between the Gaussian mean and the expected energy.

For the coincidence measurements, the time difference between the detection of two simultaneously produced back-to-back photons has been evaluated by the DAQ and stored. The time difference is always calculated as the time of detection in detector A, t_A, minus the time of detection in detector B, t_B, and is positive when $t_A > t_B$ of and negative vice versa.

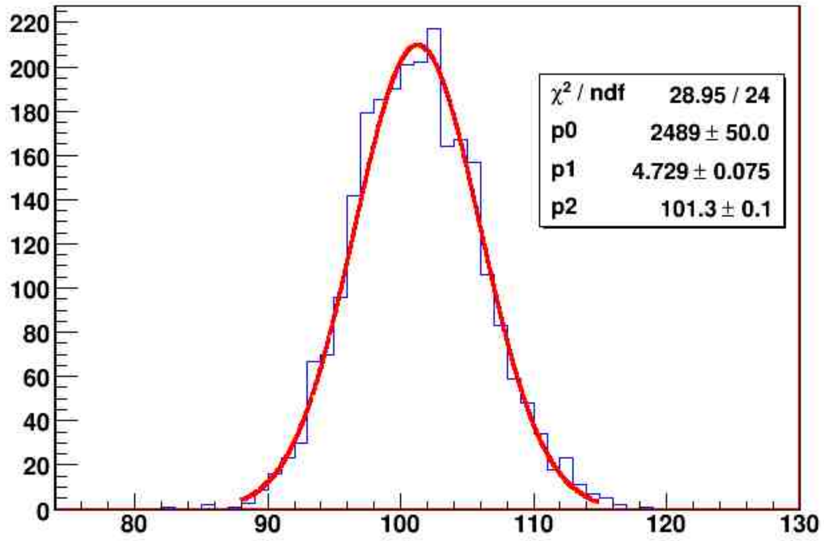

Figure 2.4: Example of noise distribution and a Gaussian fit applied on it. Events selected with a random Trigger.

2.3 Measurement of the Mobility for Electrons and Holes

Mobility of charge carriers in a semiconductor diode plays a very important role in the timing performance of the overall semiconductor detector. The output signal of the preamplifier has been used to measure it. It typically consists of two very well differentiated slopes, the first one corresponding to the induced charge to both electrons and holes and the second one only due to holes. Apply a linear fit to each of them is a method to obtain the velocity for the carriers and thus, the mobility. A crucial assumption of this method is that the time constant of the RC circuit represented by the preamplifier is big enough to be neglected when compared to the drift time of the charge carriers. Though this assumption is in general true for electrons, it can be non valid in the case of holes whose drift time is of the order of few hundreds of nanoseconds. A discussion about the bias introduced by neglecting a non-big-enough RC time constant is in section 3.4.

In Fig. 2.5 the output signal of the preamplifier of one event and the linear fits applied on both slopes are shown. The first slope (blue) is due to electron and holes induction and the second one (red) only to holes, the value for the normalized velocities (v′) are shown in eq 2.1 and eq 2.2.

$$v'_{h^+} = a_{red} = (8.3 \pm 17.1)10^{-4} \text{ Detector thickness/ns} \tag{2.1}$$

$$v'_{e^-} = a_{blue} - a_{red} = (3.07 \pm 0.42)10^{-2} \text{ Detector thickness/ns} \tag{2.2}$$

These values correspond to the normalized drift of the charge carriers along the diode so they have to be multiplied by the detector thickness to obtain a real distance over time magnitude (eq 2.3).

$$v = v'\Delta x \tag{2.3}$$

The mobility is the ratio of the velocity over the spatial normalised bias voltage (V/Δx), the value for both charge carriers is evaluated in eq 2.4 and 2.5.

$$\mu_{h^+} = \frac{v_{h^+}\Delta x}{V} = 66\ cm^2/V \cdot s \tag{2.4}$$

$$\mu_{e^-} = \frac{v_{e^-}\Delta x}{V} = 2456\ cm^2/V \cdot s \tag{2.5}$$

The $\mu\tau$ products can be evaluated taking the mobility values together with the lifetime ones quoted in [11], the results are shown in eq 2.6 and eq 2.7. These results are coherent with the ones measured for CdTe detectors of similar size in [12, 13, 14, 15, 16].

$$\mu_{h^+}\tau_{h^+} = 66 \cdot 2 \cdot 10^{-6} = 1.32 \cdot 10^{-4}\ cm^2/V \tag{2.6}$$

$$\mu_{e^-}\tau_{e^-} = 2456 \cdot 3 \cdot 10^{-6} = 7.37 \cdot 10^{-3}\ cm^2/V \tag{2.7}$$

2.4 Measurement of the Energy Resolution

Spectroscopies of ^{57}Co and ^{22}Na radioactive sources under different conditions of bias voltage and temperature have been taken to measure the energy resolution of the detector at different energy levels. ^{57}Co has its most likely line of emission at 122 keV, whether the ^{22}Na has it at 511 keV. These energies are of importance because they are very close to the two most common radionuclides used in SPECT and PET respectively, which are ^{99}Tc-MDP[1] (141 keV) and ^{18}F-FDG[2] (511 keV), respectively.

---

[1] ^{99}Tc-Methyl diphosphonate

[2] ^{18}F-Fluorodeoxyglucose

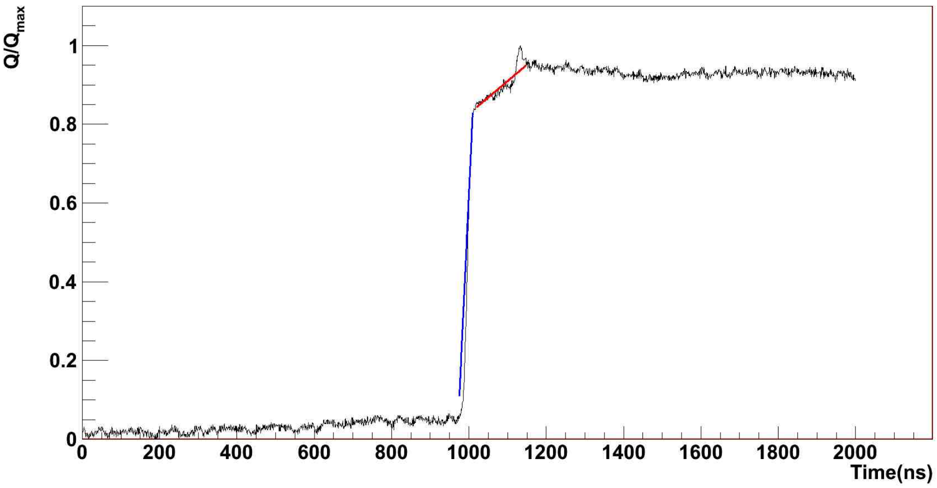

Figure 2.5: Preamplifier output signal for an event, vertical scale normalized to the maximum charge. Linear fit parameters, y=ax+b, $a_{blue}=(3.15\pm0.25)10^{-2}$, $a_{red}=(8.3\pm17.1)10^{-4}$.

In many publications, the way to measure the energy resolution consists of applying a fit on the peak and taking the FWHM of the fit as the ΔE. However, in semiconductor detectors, the shape of the peak is not symmetric due to the tail created by the extra trapping suffered by hole-dominated events. In this work it has been decided to measure the exact width at half the height of the maximum bin because it has been considered to be a fairer method.

2.4.1 Resolution at 122 keV

The decay scheme of ^{57}Co is shown in Fig. 2.6. One can see that the 122 keV line is the most likely to detect.

In Fig. 2.7 a spectroscopy at 500 V/mm and at room temperature is shown. A 3.03% resolution for the 122 keV line is achieved. This result is a factor 2 better than the one presented in [17] for a 2 mm thickness CdTe detector, because of a significant reduction of the charge trapping tail. A closer result is obtained in [12] (3.7%) for a 10 mm thickness CdTe detector operated at 1500 V, an improvement to 2.7% is also shown for a 4 mm CdTe detector which is comparable to the result achieved on this work. A clearly better resolution around 2% is presented in [18] for a 1.2 mm thickness CdTe detector operated at 1000 V. In order to obtain a result closer to this last one, the detector has been operated at 1000 V/mm and kept at -8°C to reduce the increase of the leakage current that this produces. The final resolution measured is of 2.62%, see Fig. 2.8, this result is better than any found in the literature but [18] because the thickness on the detector in that case is of 1.2 mm. The thinner the detector is the most weak is the effect of the charge trapping and the better is the resolution, so its acceptable to find such results for such better conditions.

2.4.2 Resolution at 511 keV

The decay scheme for ^{22}Na is shown in Fig. 2.9. As one can see, the most probable channel of emission is the β^+ that leads to the excited state of the ^{22}Ne, which will immediately emit a 1275 keV gamma to reach its ground state. Since the β^+ will annihilate with an electron,

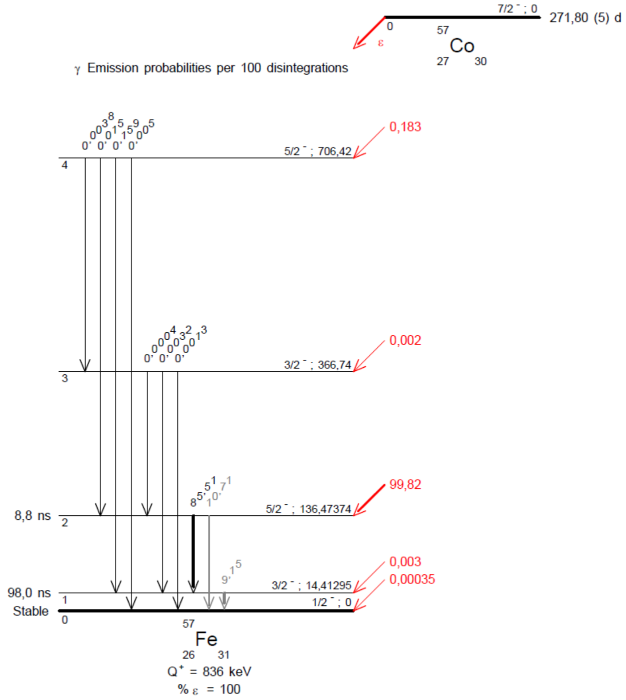

Figure 2.6: ^{57}Co disintegration diagram.

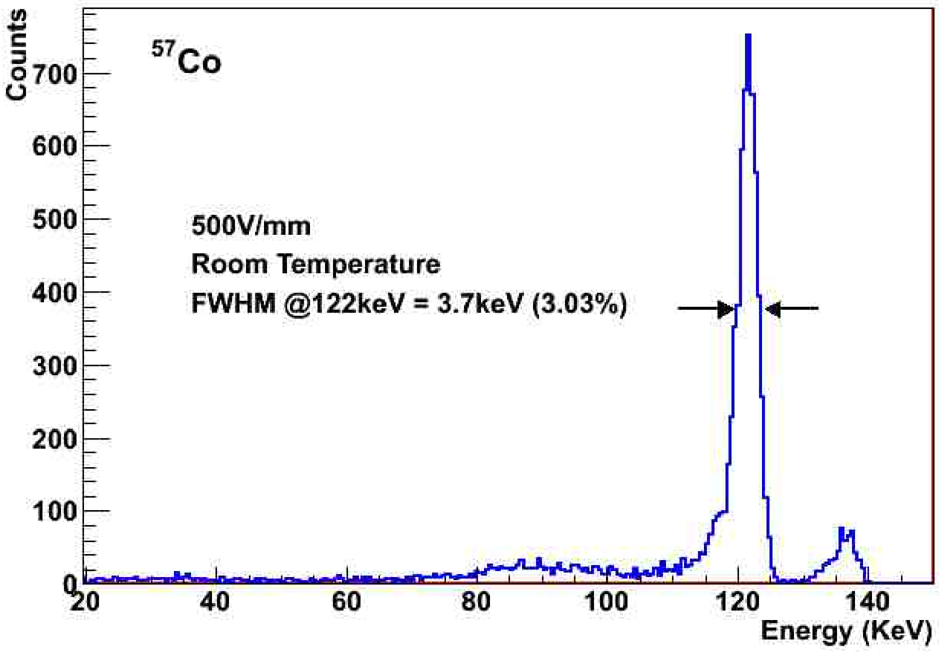

Figure 2.7: ^{57}Co spectroscopy at 500 V/mm at room temperature. FWHM=3.7 keV at 122 keV line, 3.01% resolution.

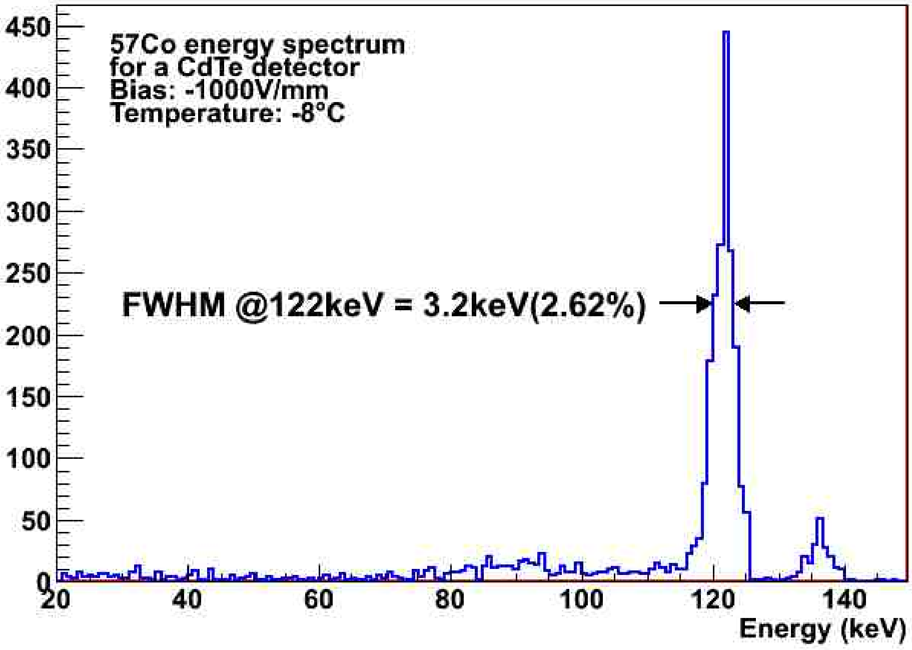

Figure 2.8: ^{57}Co spectroscopy at 1000 V/mm at -8°C. FWHM=3.2 keV at 122 keV line, 2.62% resolution.

the ^{22}Na spectroscopy will show two lines, the most probable at 511 keV and another at 1275 keV. Given that only the energy resolution at 511 keV is interesting for the PET purpose, the analysis has been focused on this line.

Fig. 2.10 shows a spectroscopy of the ^{22}Na source with a bias voltage of 500 V/mm and at room temperature. The resolution achieved is of 1.57% (8 keV FWHM) at the 511 keV line. This result is better by at least a factor 2 than the ones presented on [19, 20, 21]. It is comparable to the one in [22], for a stacked detector of 0.5 mm thick CdTe layers biased at 300 V and -20°C which is of 1.47% (7.5 keV FWHM). As in the case of the ^{57}Co, the bias voltage has been increased to 1000 V/mm and the detector has been cooled down to -8°C and the resolution has been improved to 0.98% (5 keV FWHM). This is very close to the results in [23] which are of 0.8% (4 keV FWHM) for a CdTe detector of 0.5 mm thickness, operated at 800 V and at 5°C. The combination of (small) thickness and (high) bias voltage becomes important to achieve a great energy resolution.

2.5 Measurement of the Coincidence Time Resolution

Coincidence time resolution is a crucial feature to proof that CdTe detectors can be successfully used in PET. Coincidence time resolution has been measured for two identical CdTe detectors at low temperature and 1000 V/mm bias voltage. Every coincidence consists of two hits (one on each detector), the energy for both of them as well as the difference between the detection times have been taken. The threshold has been kept always at the equivalent of 25 keV on the preamplifiers' output signal. Once the data has been taken, coincidences have been selected depending on minimum acceptance energies, in a range from 25 keV to 500 keV. The FWHM as well as the time window containing 70% and 90% of the coincidences of the distribution have been measured, the value of this magnitudes versus the minimum acceptance energies is shown

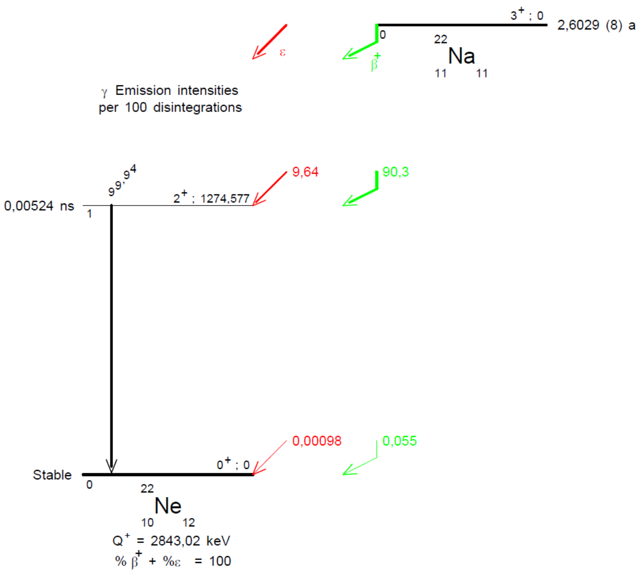

Figure 2.9: ^{22}Na disintegration diagram.

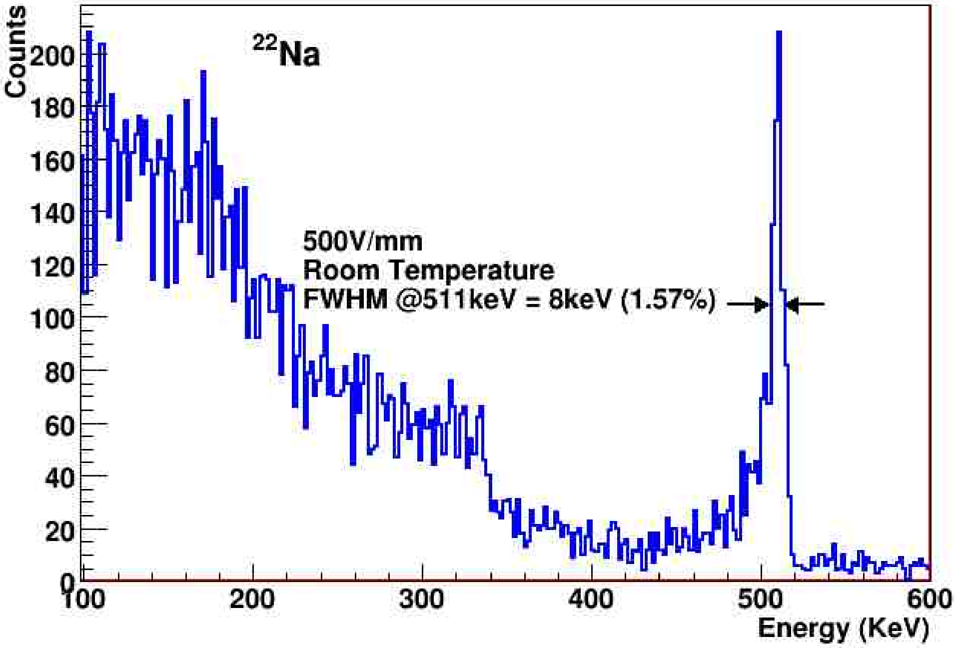

Figure 2.10: ^{22}Na spectroscopy at 1000 V/mm and at -8°C. FWHM = 8 keV at 511 keV line, 1.57% resolution. Results presented on IEEE NSS/MIC and RTSD Workshop in Valencia, October 2011 [24].

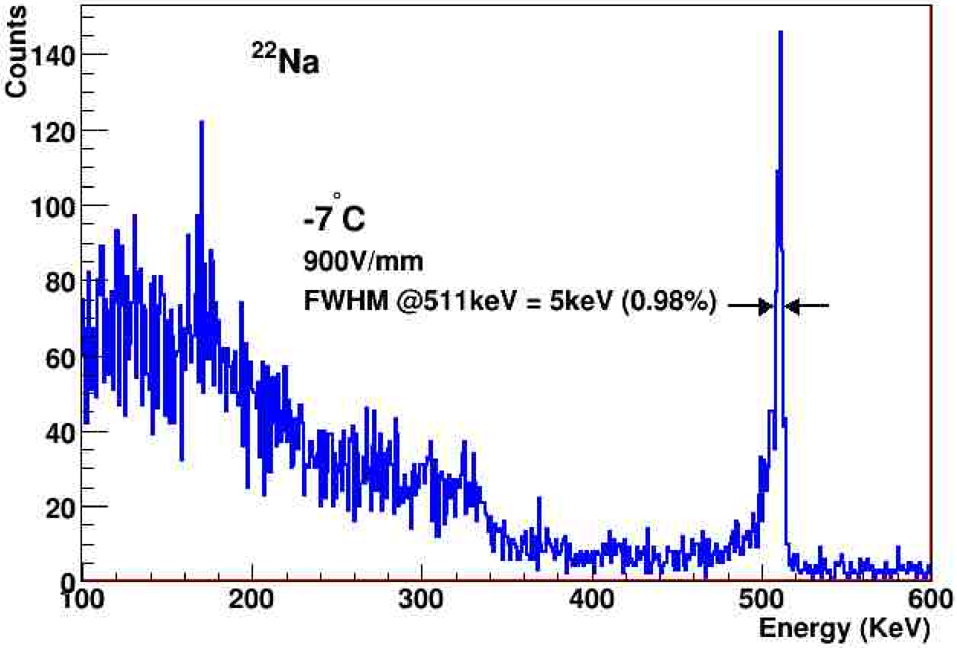

Figure 2.11: ^{22}Na spectroscopy at 500 V/mm and room temperature. FWHM=5 keV at 511 keV line, 0.98% resolution. Results presented on IEEE NSS/MIC and RTSD Workshop in Valencia, October 2011 [24].

in Fig. 2.12a. The distributions for the representative cases of the maximum and minimum of the minimum acceptance energy are shown in Fig. 2.12c and Fig. 2.12d respectively.

The results for the minimum acceptance energy (25 keV) show a 12.5 ns FWHM, which is more than 3 times better than the results presented in [5, 21] for similar setups. [19, 20] both show a 13.8 ns FWHM on the coincidence time distribution for 2 mm and 1 mm thickness respecticely and at low temperature. A slightly better result is shown in [25] for a 0.5 mm thickness CdTe detector biased at 800 V, the FWHM is of 9 ns. Compraable results to this one are obtained for higher values of the minimum acceptance energy down to 6 ns for the 500 keV acceptance energy.

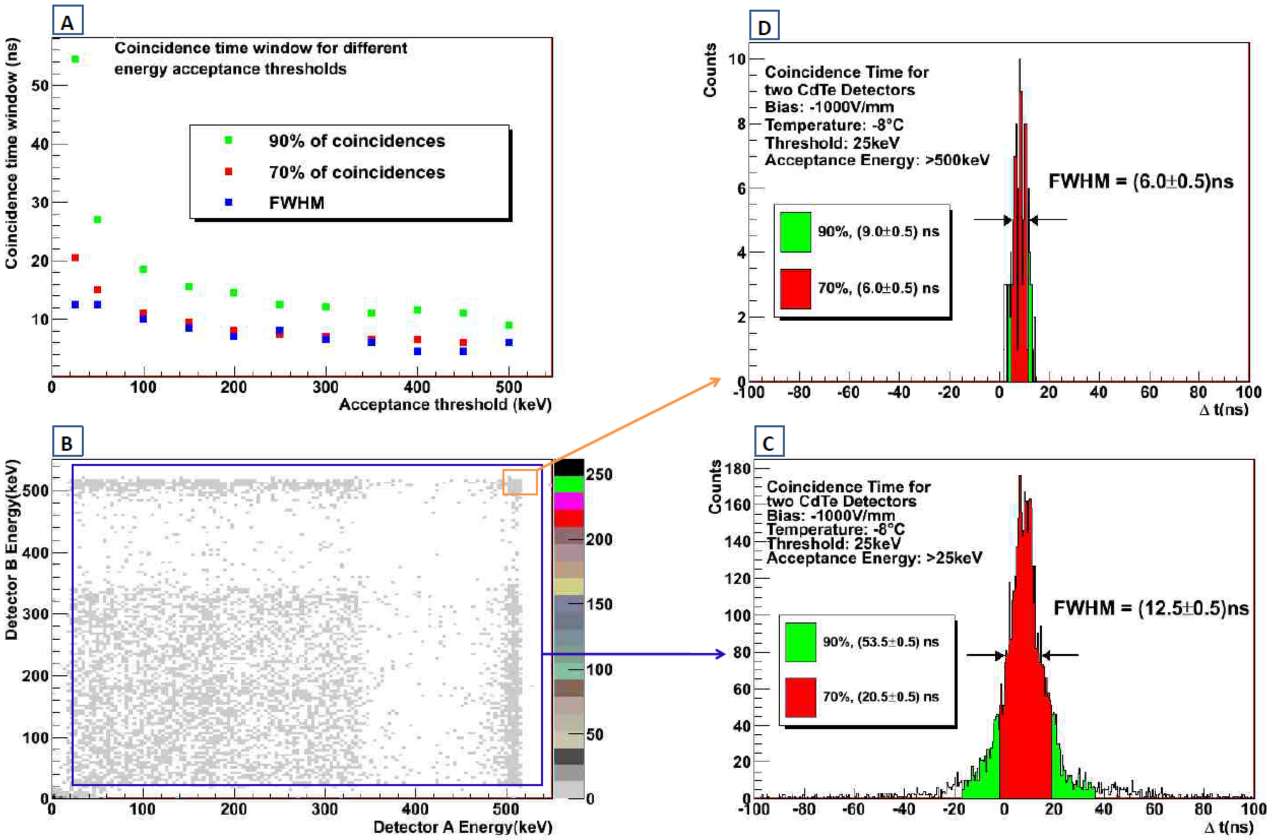

Figure 2.12: a) FWHM, 70% population time window and 90% population time window for coincidence time distribution with a given acceptance energy vs the minimum acceptance energy; b) scatter plot of the energy of the hits in every coincidence; c) coincidence time distribution for a minimum acceptance energy of 25 keV; d) coincidence time distribution for a minimum acceptance energy of 500 keV. Results presented on 14th iWoRID Workshop in Coimbra (Portugal), July 2012. [26].

Chapter 3

Monte Carlo Simulation

In order to be able to extend the results from a single detector to the case of the full PET, the conditions of the setup have been reproduced. At the moment, only the experiments of spectroscopy and timing with the ^{22}Na source have been simulated.

A combination of different programming environments has been used for this purpose. The Geant4-based Architecture for Medicine-Oriented Simulations (GAMOS) [27] has been employed for the definition of the geometry and the simulation of the interaction between radiation and matter. GAMOS has been specifically developed for those users interested in simulating Medical Physics applications using GEANT4 in a fast-to-learn and user friendly framework, though the full range of GAMOS possible applications spans well beyond the Medical Physics field. In this work, GAMOS has been used to simulate the emission of different radioactive sources and to provide the information of energy, space, and time resulting from the interaction between the radiation and the detector.

A second step of the simulation involved the development of a C++ code to model the drift of the charge carriers through the CdTe detectors and the formation and processing of the electronic signal. In particular the preliminary version of the code used for the results presented in this thesis could account for the effects of charge trapping, charge induction, and electronic noise. A new version of the software is being developed and will finally include the effects of the signal amplification and shaping for a more realistic model of the output signal.

Finally, a large number of simulated events for different setup conditions have been collected, analyzed, and compared to the real data for an assessment of the precision of the simulation and to obtain indications for a tuning of the simulation models and parameters.

3.1 Simulation of the Experimental Setup

The full spectrum of the events detected by our CdTe detector depends in general on the physics laws describing the interaction of particles and matter and more in particular it depends on the emission spectrum of the source, the geometry of the source, the geometry of the detector, and the amount and distribution of the material in the surrounding. All this characteristics can be accurately modeled using the GAMOS simulation framework.

It is of great importance to reproduce carefully the objects close to the source and the detector to simulate properly the number and the position of the positron annihilations as well as the number of photons interacting with some passive material before hitting the detector. A mistake in the definition of the dimensions or density of the objects can lead to a considerable difference between the simulated and the detected energy spectra. Nevertheless, several assumptions have been introduced to simplify the geometry description and a study of the systematic uncertainty introduced by such simplifications is on going.

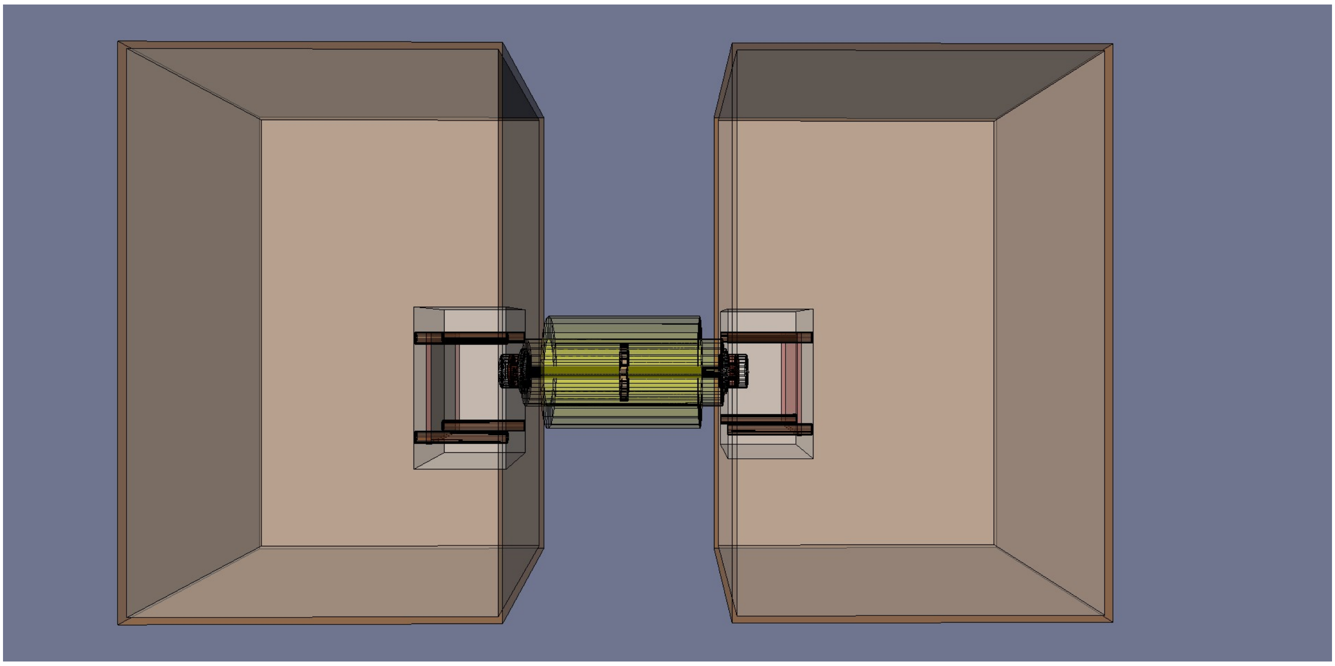

Figure 3.1: Geometry of the setup defined with GAMOS.

The picture of the complete setup as defined in GAMOS is shown in Fig. 3.1. This can be compared with the picture of the real one shown in Fig. 2.1. In particular, the radiation source case and the source shielding have been precisely modeled following the manufacturer specifications in Fig. 3.3 and Fig. 3.4. The two identical detector containers have been defined as simple alluminum boxes with 2 mm thick walls. Apart from the detectors, only those electronic components in the vicinity of the detector have been added: the PCBs where the detectors are mounted, the cylinders holding the detectors, and the screws of the PCB. All these components are mimicked with simple geometrical shapes (parallelepiped or cylinder) and with uniform density materials. Other objects inside the aluminum box placed farther from the detector (wires or other PCBs) have not been simulated.

3.2 Simulation of the Interaction between Radiation and Matter

The active region of the source volume is filled with ^{22}Na with an activity of $2.17{\cdot}10^2$ Bq. Only two decay channels are considered for ^{22}Na (see Fig. 2.9): the positron emission with an energy of 215.5 keV and a probability of 90.5%, and the gamma emission with an energy of 1275 keV and a probability of 99.95%. Further studies are necessary to assess the effect of considering only a single emission energy for the emitted positrons instead of the characterstic broad spectrum with energies up to 540 keV and resulting enhanced penetration power. The standard electromagnetic and hadronic physics tables are used as defined in the Geant4 manual [28] with standard range cut for the production of secondary particles. Given the involved energies, the simulation of the interaction particle-matter in Geant4 is expected to be very accurate.

For every particle and interaction, GAMOS offers a huge list of magnitudes to be recorded. For the purpose of our study, only the position, time and deposited energy correspondent to any interaction in any of the two detectors are saved. An example of the spectrum of the energy deposited in the CdTe is shown in Fig. 3.5. The 511 keV and the 1275 keV peaks are very well visible, together with escape peaks and the compton edges for the two energies.

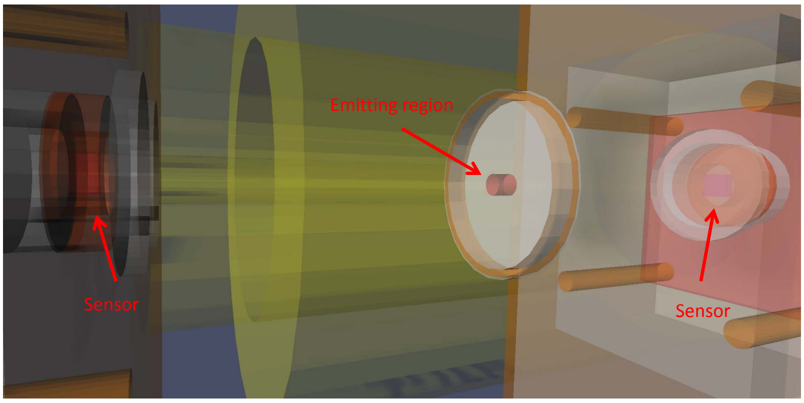

Figure 3.2: Short frame of the central part of the setup.

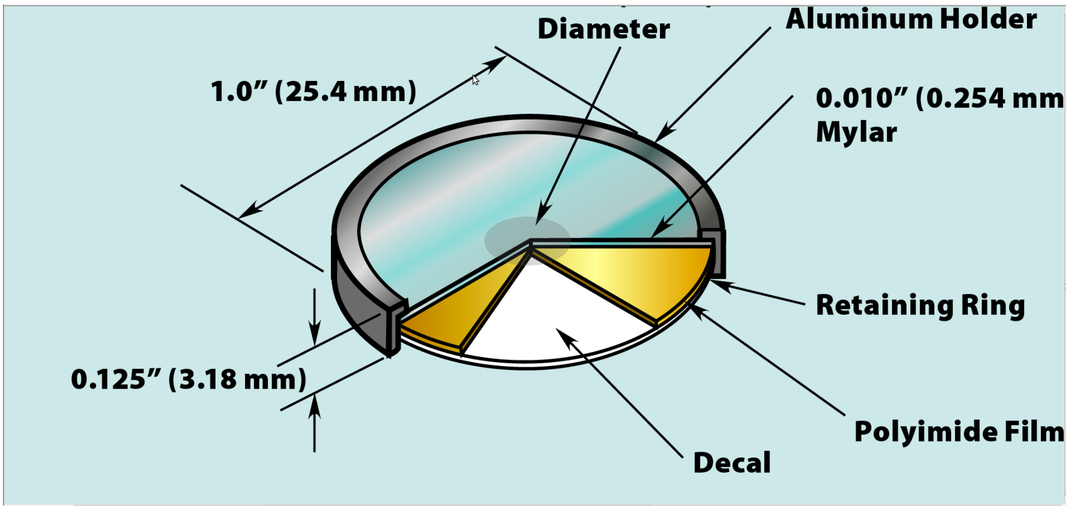

Figure 3.3: Radiation case specifications of the ^{22}Na radioactive source.

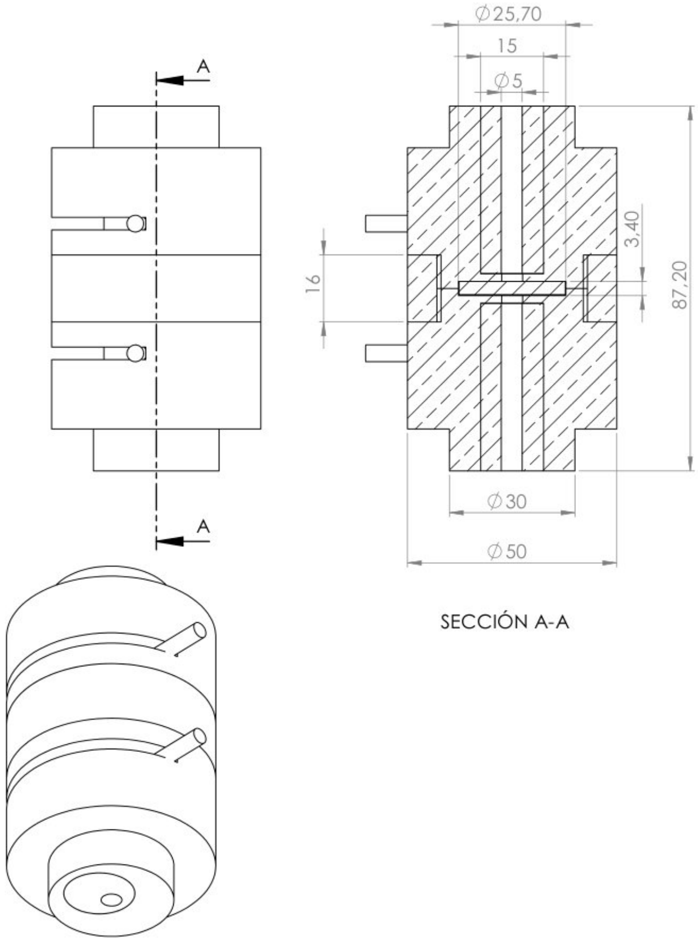

Figure 3.4: Specifications of the radiation source shielding.

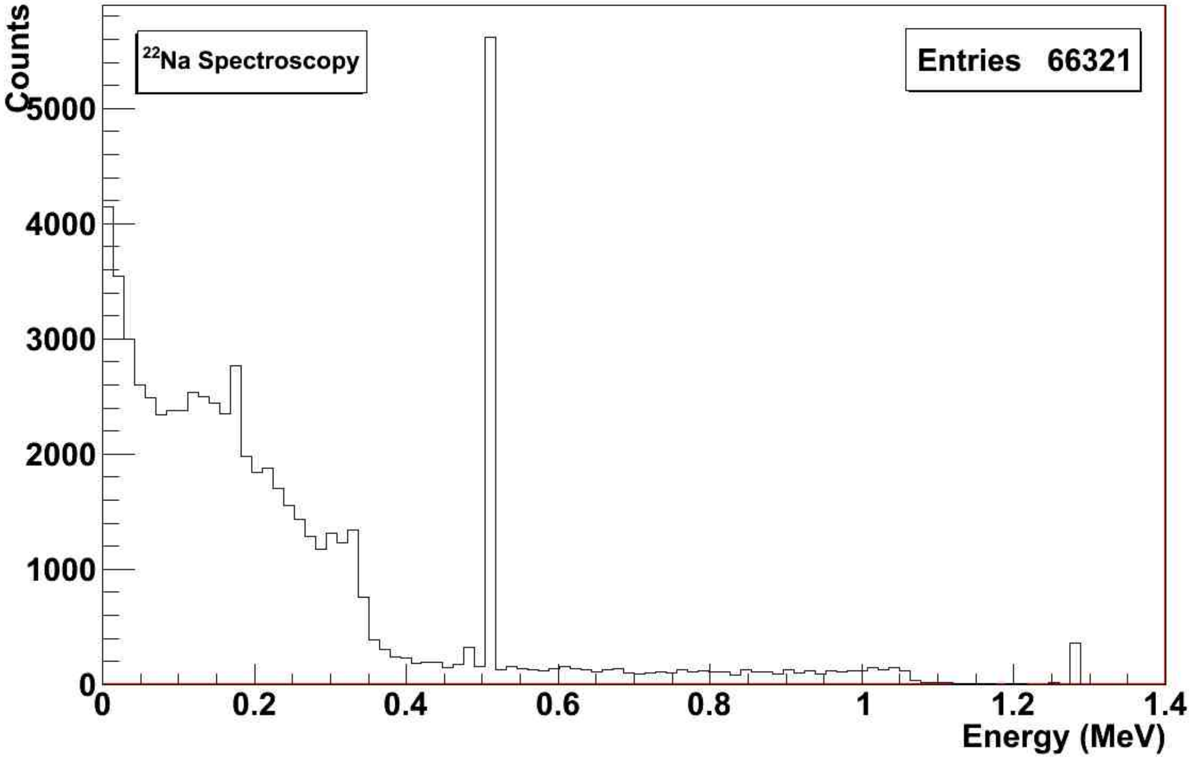

Figure 3.5: Spectrum of the energy deposited in the CdTe generated by GAMOS.

The energy spectrum as shown in Fig.3.5 would be the exact output of a perfect detector with zero energy resolution. In the real life several factors involved in the signal formation and processing would contribute to the smearing of the measured energy. How these effects are included in the simulation is explained in the next section.

3.3 Simulation of the Signal Formation and Processing

The different steps from the energy deposition in the CdTe to the final output signal, namely the creation of the charge carriers, the drift and trapping of the carriers through the detecor, the charge collection, the signal preamplification, the energy trigger, and the signal shaping, are described in details in section 1.2. To model correctly all this processes is a very difficult task and requires a careful fine tuning of the simulation parameters and the correct assessment of the systematic introduced by the assumption on the chosen physics models. For this thesis only a preliminary version of such simulation has been completed with limited functionality and precision and no estimation of the systematic uncertainty is yet available. Nevertheless, our program can already take into account for the charge drifting and trapping, the charge collection, and the energy trigger and provides a correct simulation of the electronic noise. Further effort is being dedicated to include the effect of the signal amplification and shaping that play a crytical role in moulding the final energy spectrum. The assumptions on the simulation of the signal formation and processing chain are detailed in the following.

The GAMOS output data gives the 3D position, time and deposited energy for every interaction in the detector. It is known that the free-electrons generated form a cloud around the

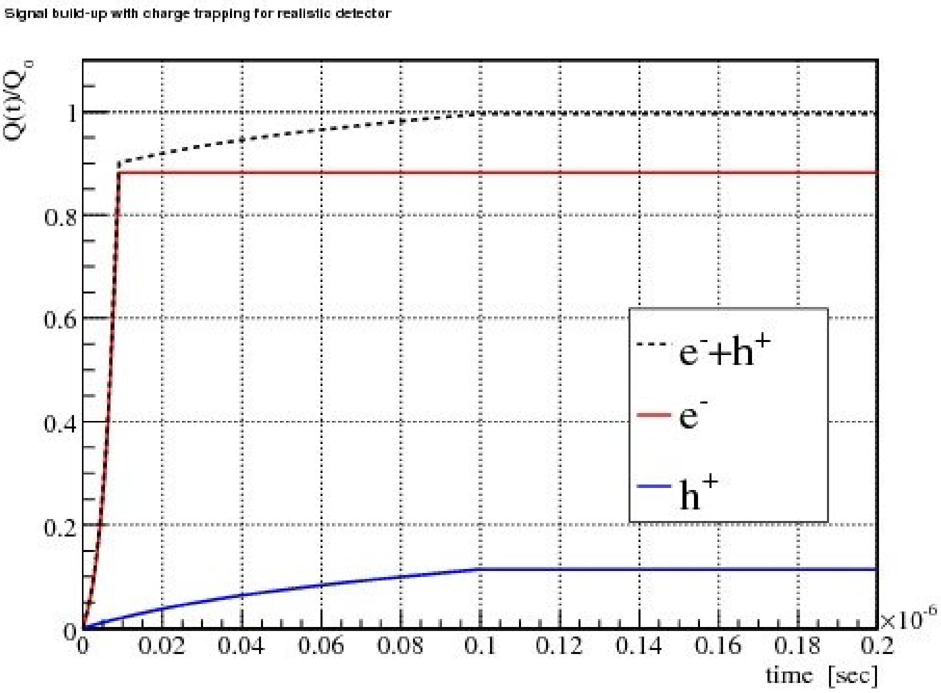

Figure 3.6: Simulated induced charge for the two electrodes separately and the sum of them. e$^-$ collection corresponds to the cathode collection and h+ to the anode.

μ_{e^-}	2456 cm^2/V s
μ_{h^+}	66 cm^2/V s
τ_{e^-}	3 μs
τ_{h^+}	2 μs

Table 3.1: Mobility and mean life-time parameter values for electrons and holes used in the simulation.

interaction point, for simplicity, all these electrons have been considered to lie in a point. The detector has been meshed, the closest node to the *real* interaction point has been taken as the starting point.

The charge drift has been represented as the jumps between consecutive nodes. In every node the trapped charge and the induced charge have been evaluated. A plot of time vs total induced charge on the electrode has been obtained. The sum of this plot for the two electrodes (anode and cathode), where each of them corresponds to the collected charge due to a different charge carrier, is shown in Fig. 3.6

Hecht equation (eq 1.10) has been used to evaluate the charge trapping. The parameters used are shown in table 3.1. The method described in [4] has been used to evaluate the charge induction on the electrodes. A random value from a zero-mean gausian distribution with $\sigma = \sigma_{noise}$ has been added to the final induced charge in order to model the electronic noise.

3.4 Results

Preliminary results include the comparison between the simulated and real energy spectra in Fig. 3.7 and the simulated and real distributions of the time difference between simultaneous

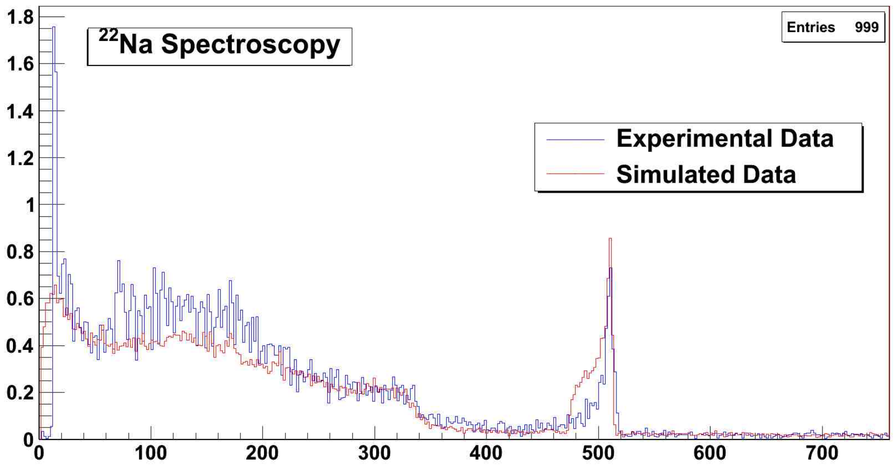

Figure 3.7: Spectroscopy of the deposited energy with the implementations mentioned in section 3.3 (red) and the measured with the setup (blue).

511 keV back-to-back photons detected by the two detectors in Fig. 3.8. Both energy and time comparisons show significant discrepancies between real and simulated data. The possible causes behind such discrepancies are discussed in the following and are driving the current development of the simulation software.

3.4.1 Energy Spectrum

Data and Monte Carlo distributions are normalized such to have the same number of detected events in the energy sideband defined as the interval between 600 keV and 700 keV. After normalization, the total number of expected and observed events agree as integrated over the full energy spectrum down to 220 keV. Below such threshold, real data show a clear excess probably due to the double effect of a possible misalignment of the source with respect to the detector and an underestimation of the amount of passive material around the detector. The Compton edge of the 511 keV photons, expected to be at around 340 keV, is correctly reproduced in terms of shape and number of events, as well as the flat contribution of Compton scattered 1275 keV photons in the region above 520 keV.

The 511 keV peak shows two different problems. On the one hand, a clear excess of events in the low energy tail immediatly below the peak value (from 475 to 511 keV) indicates a possible overestimation of the charge trapping effect. On the other hand, the amount of real data is systematically bigger than simulation right above the Compton edge, i.e. in the region between 350 and 475 keV, even though the integrated number of events in the full peak region (from 350 to 550 keV) is the same for real and simulated data. A possible explanation of this dual discrepancy is the lack of a realistic model for the signal formation electronic chain, including signal pre-amplification and signal shaping as explained in section 1.2. A crucial missing parameter in the simulation is in fact the time constant of the RC circuit of the pre-amplifier. From one side, by neglecting this factor the measured value of the hole $\mu\tau$ product provided in section 2.3 ($\mu_h\tau_h = 1.32 \cdot 10^{-4}$ cm^2/V) can be underestimated with a resulting overestimation of the charge trapping effect. As an example, the energy spectrum obtained with faster holes ($\mu_h\tau_h = 1.8 \cdot 10^{-4}$ cm^2/V from measurements in [12]) gives a much narrower photopeak as shown in Fig. 3.9. On the other side, the signal attenuation due to a pre-amplifier too fast discharging propagates to

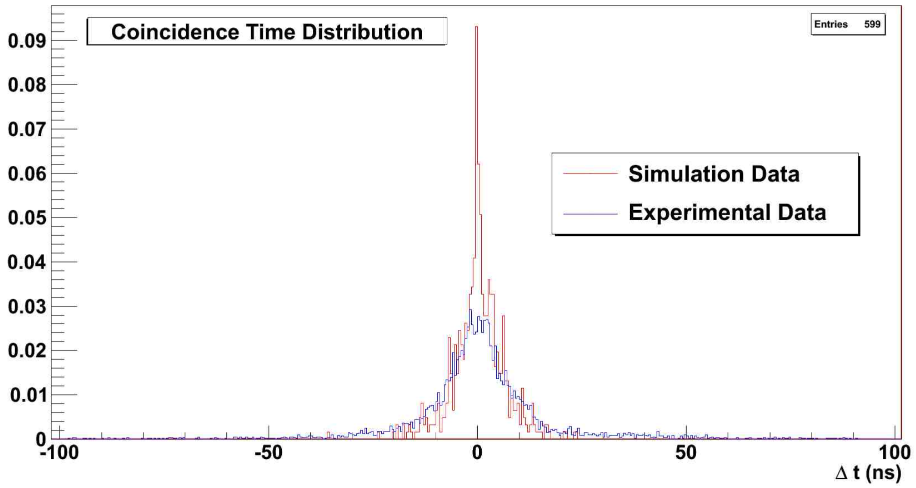

Figure 3.8: Simulation of the coincidence time distribution (red) and the measured with the setup (blue).

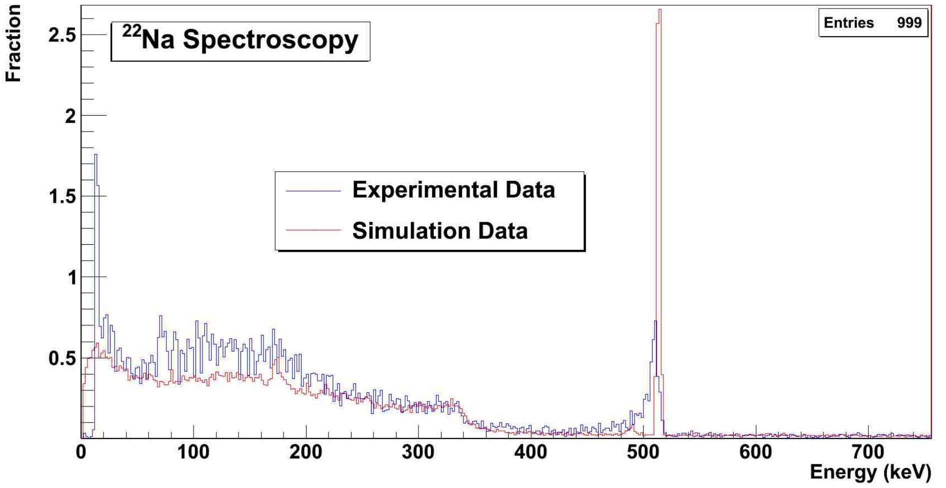

Figure 3.9: Spectroscopy of the deposited energy with the implementations mentioned in section 3.3 with the measured parameters in [12] (red) and the measured with the setup (blue).

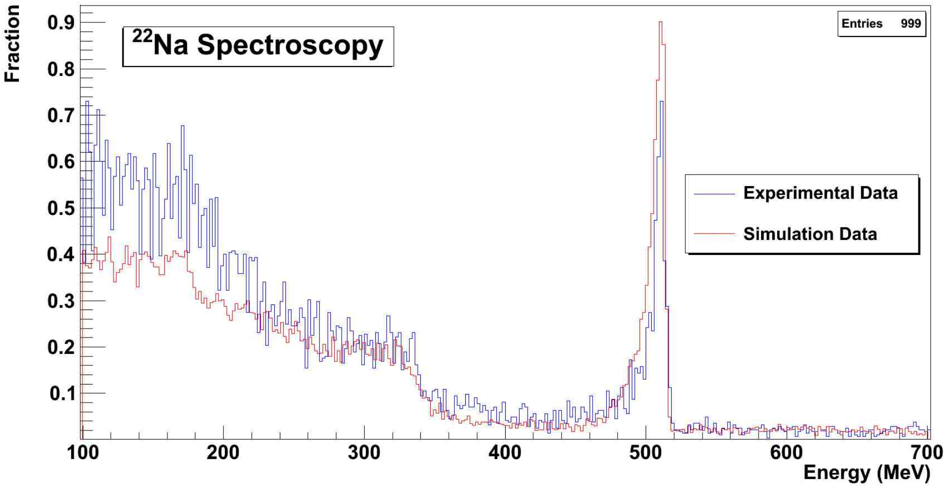

Figure 3.10: Spectroscopy of the deposited energy with the implementations mentioned in section 3.3 with the measured parameters in [12] and an extra artificial exponential attenuation (red) and the measured with the setup (blue).

the signal shaper and finally alterates the value of the energy. The effect is to have a migration of events from the peak towards lower energy values. Fig. 3.10 shows how the energy spectrum in Fig. 3.9 is modified by introducing an artificial exponential attenuation to the energy values of the photopeak events. Though a careful quantitative estimation and modelization of the RC effect is clearly necessary and currently under study, the improved agreement of Fig. 3.10 is a clear indication of the crucial role that it plays in the interpretation of our results.

3.4.2 Time Difference Distribution

Given that the two detected photons are produced by the same annihilation, the time difference between the two detections must be due to the charge collection mechanism of the CdTe twin detectors. As explained in section 1.1, the trigger time of a given event depends on the ratio between the hole and electron components of the energy necessary to reach the trigger threshold, thus ultimately depends on the depth of interaction of the interacting photon and on the amount of energy deposited.

Fig. 3.8 shows the comparison between the real and simulated distributions of the time difference between simultaneous events detected by the two detectors. The Monte Carlo distribution is clearly narrower than the correspondent distribution from real data. As for the discrepancies in the spectroscopy, the difference can still be due to the overestimation of the preamplifier time constant. An attenuation of the preamplifier signal would in fact increase the trigger time and consequently broaden the time difference distribution.

Chapter 4

Conclusions

This master thesis reports on the characterization of a single channel CdTe diode detector with Shottcky contact with the aim of proving the feasibility of using such detector for PET applications.

A complete setup has been built in the laboratory in order to test the CdTe detector in the range of conditions expected for the full PET device. Such conditions include the control and variation of temperature, bias voltage, and radiation energy. The development of ad-hoc data adquisition (DAQ) and data analysis software has been an essential part of the work.

The main experimental results include:

- the measurement of the mobility of electron and holes in the CdTe with μ_e=2456 cm^2/V s and μ_h=66 cm^2/V s
- the measurement of the energy resolution with
  $E_{FWHM}(E_g$=122 keV, T=25°C, V=500 V/mm)=3.7 keV,
  $E_{FWHM}(E_g$=122 keV, T=-8°C, V=1000 V/mm)=3.2 keV,
  $E_{FWHM}(E_g$=511 keV, T=25°C, V=500 V/mm)=8 keV
  $E_{FWHM}(E_g$=511 keV, T=-7°C, V=1000 V/mm)=5 keV.
- the measurement of the coincidence time resolution with Δt=12.5 ns for E>25 keV and Δt=6 ns for E>500 keV

These results are compatible with similar findings available in literature [5, 12, 18, 19, 20, 21, 23, 25] and prove the excellent potential of CdTe for PET applications.

In parallel, a full simulation of the experimental setup has been developed and tested against the collected data. A reliable simulation is of crucial importance to be able to extend the results of the characterization of a single CdTe detector to the case of a full PET scanner with $O(10^6)$ channels. Preliminary results have been provided in terms of comparison of energy and timing distributions between simulated and real data. A careful study of the spotted discrepancies is on going and will drive future improvement of the Monte Carlo software towards an as realistic as possible simulation.

The results presented in this thesis have provided vital information for the development of the front end electronic that will be employed in the PET prototype being built by the VIP group. Furthermore, this work constitutes the essential basis of any further characterization of CdTe systems of higher complexity. The natural next step is to extend this results to the case of a multichannel detector with the CdTe volume segmented into mm size pixels. The laboratory setup is already being modified towards the multichannel measurements and a new version of the DAQ software in under commisioning.

Bibliography

[1] O. D. Kellog. *Foundations of Potential Theory.* New York: Frederick Ungar Publ.Co., 1929, p 230.

[2] S. Ramo. Currents induced by electron motion. *Proceedings of the IRE*, 27(9):584 – 585, sept. 1939.

[3] W. Shockley. Currents to conductors induced by a moving point charge. *Journal of Applied Physics*, 9(10):635 –636, oct 1938.

[4] Uri Lachish. Driving spectral resolution to the noise limit in semiconductor gamma detector arrays. In *IEEE Transactions on Nuclear Science*, volume 48, June 2001.

[5] R. Amrami, G. Shani, Y. Hefetz, A. Pansky, and N. Wainer. Timing performance of pixelated cdznte detectors. *Nuclear Instruments and Methods in Physics Research Section A: Accelerators, Spectrometers, Detectors and Associated Equipment*, 458(3):772 – 781, 2001.

[6] P.E. Valk D. Delbeke D.L. Bailey D.W. Townsend and M.N. Maisey (Eds). *Positron Emission Tomography. Clinical practice.* Springer-Verlag London Limited 2010, Lexington KY, 2011.

[7] O. Warburg. On the origin of cancer cells. *Science*, (123):306–314, 1956.

[8] Gopal B. Saha. *Basics of PET imaing. Physics, chemistry and regulations.* Springer Science+Business Media, Inc. New York, 2005.

[9] M. Chmeissani, P. Arce, and M. Canadas. Modeling and simulation of pet scanner based on pixelated solid-state detector. In *Nuclear Science Symposium Conference Record (NSS/MIC), 2009 IEEE*, pages 3496 –3502, 24 2009-nov. 1 2009.

[10] Main page of the ROOT Project. http://root.cern.ch/drupal/.

[11] Table of electrons and holes lifetimes for CdTe and CdZnTe. http://www.amptek.com/anczt2.html.

[12] Y. Eisen, A. Shor, and I. Mardor. Cdte and cdznte gamma ray detectors for medical and industrial imaging systems. *Nuclear Instruments and Methods in Physics Research Section A: Accelerators, Spectrometers, Detectors and Associated Equipment*, 428(1):158 – 170, 1999.

[13] E. Bertolucci, M. Conti, C.A. Curto, and P. Russo. Timing properties of cdznte detectors for positron emission tomography. *Nuclear Instruments and Methods in Physics Research Section A: Accelerators, Spectrometers, Detectors and Associated Equipment*, 400(1):107 – 112, 1997.

[14] G. Sato, T. Takahashi, M. Sugiho, M. Kouda, T. Mitani, K. Nakazawa, Y. Okada, and S. Watanabe. Characterization of cdte/cdznte detectors. *Nuclear Science, IEEE Transactions on*, 49(3):1258 – 1263, jun 2002.

[15] Z. He, G. F. Knoll, and D. K. Wehe. Direct measurement of product of the electron mobility and mean free drift time of cdznte semiconductors using position sensitive single polarity charge sensing detectors. *Journal of Applied Physics*, 84(10):5566–5569, 1998.

[16] C. Matsumoto, T. Takahashi, K. Takizawa, R. Ohno, T. Ozaki, and K. Mori. Performance of a new schottky cdte detector for hard x-ray spectroscopy. *Nuclear Science, IEEE Transactions on*, 45(3):428 –432, jun 1998.

[17] C Scheiber. Cdte and cdznte detectors in nuclear medicine. *Nuclear Instruments and Methods in Physics Research Section A: Accelerators, Spectrometers, Detectors and Associated Equipment*, 448(3):513 – 524, 2000.

[18] T. Takahashi, T. Mitani, Y. Kobayashi, M. Kouda, G. Sato, S. Watanabe, K. Nakazawa, Y. Okada, M. Funaki, R. Ohno, and K. Mori. High-resolution schottky cdte diode detector. *Nuclear Science, IEEE Transactions on*, 49(3):1297 – 1303, jun 2002.

[19] Yiping Shao, H. Bradford Barber, Stephen J. Balzer, and Simon R. Cherry. Measurement of coincidence timing resolution with cdte detectors. volume 4142, pages 254–264. SPIE, 2000.

[20] Karl-Ludwig Giboni, Elena Aprile, Tadayoshi Doke, Masahiko Hirasawa, and Mikio Yamamoto. Coincidence timing of schottky cdte detectors for tomographic imaging. *Nuclear Instruments and Methods in Physics Research Section A: Accelerators, Spectrometers, Detectors and Associated Equipment*, 450(2-3):307 – 312, 2000.

[21] F. Casali, D. Bollini, P. Chirco, M. Rossi, G. Baldazzi, W. Dusi, E. Caroli, G. DiCocco, A. Donati, G. Landini, and J.B. Stephen. Characterization of small cdte detectors to be used for linear and matrix arrays. *Nuclear Science, IEEE Transactions on*, 39(4):598 –604, aug 1992.

[22] S. Watanabe, T. Takahashi, Y. Okada, G. Sato, M. Kouda, T. Mitani, Y. Kobayashi, K. Nakazawa, Y. Kuroda, and M. Onishi. Cdte stacked detectors for gamma-ray detection. *Nuclear Science, IEEE Transactions on*, 49(3):1292 – 1296, jun 2002.

[23] Tadayuki Takahashi, Biswajit Paul, Kazuyuki Hirose, Chiho Matsumoto, Ryouichi Ohno, Tsutomu Ozaki, Kunishiro Mori, and Yoshihiro Tomita. High-resolution schottky cdte diode for hard x-ray and gamma-ray astronomy. *Nuclear Instruments and Methods in Physics Research Section A: Accelerators, Spectrometers, Detectors and Associated Equipment*, 436(1-2):111 – 119, 1999.

[24] G. Arino et al. Characterization of CdTe Detector for Use in PET. In *Nuclear Science Symposium Conference Record (NSS/MIC) and RTSD Workshop, IEEE*, October 2011.

[25] Y. Okada, T. Takahashi, G. Sato, S. Watanabe, K. Nakazawa, K. Mori, and K. Makishima. Cdte and cdznte detectors for timing measurements. *Nuclear Science, IEEE Transactions on*, 49(4):1986 – 1992, aug 2002.

[26] G. Arino et al. Energy and Coincidence Time Resolution Measurements of CdTe detectors for PET. In *(Submitted for publication) Interational Workshop on Radiation Imaging Detectors (iWoRID) 2012 conference record*, July 2012.

[27] Main page of the GAMOS framework. http://fismed.ciemat.es/GAMOS/.

[28] Geant4 user support webpage. http://geant4.cern.ch/support/index.shtml.